Elsevier Editorial System(tm) for Lithos
Manuscript Draft

Manuscript Number: LITHOS7914

Title: The lawsonite-glaucophane blueschists of Elba Island (Italy)

Article Type: Regular Article

Keywords: HP-LT metamorphism, blueschist facies, Northern Apennines, Elba Island, P-T pseudosection, 40Ar/39Ar geochronology.

Corresponding Author: Dr. caterina Bianco, Ph.D

Corresponding Author's Institution: University of Bari

First Author: caterina Bianco, Ph.D

Order of Authors: caterina Bianco, Ph.D; Gaston Godard; Alison Halton; Andrea Brogi; Domenico Liotta; Alfredo Caggianelli

Abstract: Evidence of high-P blueschist-facies metamorphism was found in metabasites embedded in calcschists of the Eastern Elba Island (Northern Apennines, Italy). The immobile trace elements (REEs and HFSEs) of the metabasites indicate an affinity with T-MORBs. The minerals are heterogeneously distributed in the rock, defining mafic and Ca-Al-rich microdomains inherited respectively from the pyroxene- and plagioclase-rich zones of the original doleritic rock. The highest pressure paragenesis consisted of lawsonite, aegirine-omphacite, glaucophane and chlorite. Lawsonite was replaced by pseudomorphs 0.1 mm in size, with the shape of rhombic prisms and consisting of clinozoisite with inclusions of muscovite ± albite ± quartz. The inclusions are preferentially orientated parallel to one of the diagonals of the basal rhombic sections, indicating that the two diagonals were not crystallographically equivalent, implying that the protocrystals were orthorhombic prisms with {110} faces, which is indeed the case of lawsonite. The compositions of white mica and epidote are different in the pseudomorphs (muscovite and Fe3+-poor clinozoisite) and in the matrix (phengite and Fe3+-rich epidote), indicating that the protomineral was devoid of Mg and Fe, which still points to lawsonite. Thermodynamic modelling, using the THERMOCALC software and dataset, suggests that metabasites experienced a clockwise P-T path from the lawsonite-blueschist subfacies to the epidote-blueschist subfacies, down to greenschist facies. The estimated peak pressure conditions are $P \geq 1.6$ GPa and $450 < T < 500^{\circ}C$. Glaucophane grew mainly during the lawsonite-to-epidote transition and is dated at 19.8 ± 1.4 Ma by the 40Ar/39Ar method. This evolution is interpreted in terms (i) injection of basic magmas in carbonated and pelitic sediments (early Oligocene), (ii) subduction (Oligocene), (iii) collision (early Miocene: 19.8 ± 1.4 Ma), (iv) exhumation and granite intrusion (Upper Miocene) favoured by extensional tectonics. The attribution of these rocks to the Ligurian palaeo-ocean domain is here rejected; they could rather be attributed to the western margin of the Adria plate. The eastern part of Elba Island belongs to a blueschist-facies belt that extends from Gorgona Island in the northwest to Argentario and Giglio Island in the southeast, so much of the conclusions of this study can be extended to the whole of this belt.

Research Data Related to this Submission

There are no linked research data sets for this submission. The following reason is given:
Data will be made available on request

Cover letter

Caterina Bianco
University of Bari
Via Orabona 4, 70125 Bari (Italy)
caterina.bianco86@gmail.com

April, 1 2015

Dear Editor,

I am pleased to submit an original research article entitled “The lawsonite-glaucophane blueschists of Elba Island (Italy)” by Caterina Bianco; Gaston Godard; Alison Halton; Andrea Brogi; Domenico Liotta; Alfredo Caggianelli, for your evaluation on the possibility to be published in *Lithos*.

The manuscript describes a clear evidence of high-P blueschist-facies metamorphism found in metabasites embedded in calcschists of the Eastern Elba Island (Northern Apennines, Italy) and derived from dykes and/or sills with T-MORB geochemical affinity. Thermodynamic modelling, using the THERMOCALC software and dataset, display that metabasites experienced a clockwise P-T path from the lawsonite-blueschist subfacies to the epidote-blueschist subfacies, down to greenschist facies and the estimated metamorphic conditions are $P \geq 1.6$ GPa and 450–500°C. In addition, glaucophane, formed during a deformation episode at the lawsonite-epidote transition, was dated giving an age of 19.8 ± 1.4 Ma and then attributed to the collision phase. Finally, these important results allowed to attribute the Eastern Elba Island units to the Adria plate margin and to add another piece to the Tyrrhenian HP-LT metamorphic belt extended from Gorgona Island in the northwest to Argentario and Giglio Island in the southeast.

We believe that this manuscript is appropriate for publication by Lithos because it deals with petrology and, more in detail, with PT metamorphic modeling.

This manuscript has not been published and is not under consideration for publication elsewhere.
Hoping that you can find this contribution of interest,

Sincerely,

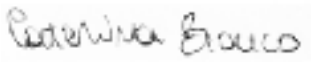

Caterina Bianco, PhD,
University of Bari

The lawsonite-glaucophane blueschists of Elba Island (Italy)

Caterina Bianco[1,*]; Gaston Godard[2]; Alison Halton[3]; Andrea Brogi[1];

Domenico Liotta[1,4]; Alfredo Caggianelli[1]

[1] University of Bari, Earth and Geo-Environmental Sciences, Via Orabona 4, 70125 Bari, Italy.

[2] Université Paris-Diderot, Institut de Physique du Globe de Paris, UMR CNRS 7154, 1 rue Jussieu, 75238-Paris cedex 05, France.

[3] Faculty of Science, Technology, Engineering & Mathematics (STEM), The Open University, Walton Hall, Milton Keynes, MK7 6AA, United Kingdom.

[4] CNR-IGG, Via G. Moruzzi 1, 56124 Pisa, Italy.

* Corresponding author: caterina.bianco@uniba.it.

Abstract

Evidence of high-P blueschist-facies metamorphism was found in metabasites embedded in calcschists of the Eastern Elba Island (Northern Apennines, Italy). The immobile trace elements (REEs and HFSEs) of the metabasites indicate an affinity with T-MORBs. The minerals are heterogeneously distributed in the rock, defining mafic and Ca-Al-rich microdomains inherited respectively from the pyroxene- and plagioclase-rich zones of the original doleritic rock. The highest pressure paragenesis consisted of lawsonite, aegirine-omphacite, glaucophane and chlorite. Lawsonite was replaced by pseudomorphs 0.1 mm in size, with the shape of rhombic prisms and consisting of clinozoisite with inclusions of muscovite ± albite ± quartz. The inclusions are preferentially orientated parallel to one of the diagonals of the basal rhombic sections, indicating that the two diagonals were not crystallographically equivalent, implying that the protocrystals were orthorhombic prisms with {110} faces, which is indeed the case of lawsonite. The compositions of white mica and epidote are different in the pseudomorphs (muscovite and Fe^{3+}-poor clinozoisite) and in the matrix (phengite and Fe^{3+}-rich epidote), indicating that the protomineral was

devoid of Mg and Fe, which still points to lawsonite. Thermodynamic modelling, using the THERMOCALC software and dataset, suggests that metabasites experienced a clockwise P-T path from the lawsonite-blueschist subfacies to the epidote-blueschist subfacies, down to greenschist facies. The estimated peak pressure conditions are $P \geq 1.6$ GPa and $450 < T < 500$°C. Glaucophane grew mainly during the lawsonite-to-epidote transition and is dated at 19.8 ± 1.4 Ma by the $^{40}Ar/^{39}Ar$ method. This evolution is interpreted in terms (i) injection of basic magmas in carbonated and pelitic sediments (early Oligocene), (ii) subduction (Oligocene), (iii) collision (early Miocene: 19.8 ± 1.4 Ma), (iv) exhumation and granite intrusion (Upper Miocene) favoured by extensional tectonics. The attribution of these rocks to the Ligurian palaeo-ocean domain is here rejected; they could rather be attributed to the western margin of the Adria plate. The eastern part of Elba Island belongs to a blueschist-facies belt that extends from Gorgona Island in the northwest to Argentario and Giglio Island in the southeast, so much of the conclusions of this study can be extended to the whole of this belt.

HIGHLIGHTS

The lawsonite-glaucophane blueschists of Elba Island (Italy)

Caterina Bianco; Gaston Godard; Alison Halton; Andrea Brogi;
Domenico Liotta; Alfredo Caggianelli

- Elba Island metabasites record metamorphic conditions of $P \geq 1.6$ GPa and 450–500°C.

- Chlorite-Lawsonite-Glaucophane-Omphacite-Rutile represents the HP-LT metamorphic assemblage.

- The transition from lawsonite-epidote to blueschist facies is dated at 19.8 ± 1.4 Ma and related to collision.

- The Rio Marina metabasites derived from dykes and/or sills with T-MORB geochemical affinity.

- The eastern Elba Island units are attributed to the margin of Adria plate.

The lawsonite-glaucophane blueschists of Elba Island (Italy)

Caterina Bianco[1,*]; Gaston Godard[2]; Alison Halton[3]; Andrea Brogi[1];
Domenico Liotta[1,4]; Alfredo Caggianelli[1]

[1] University of Bari, Earth and Geo-Environmental Sciences, Via Orabona 4, 70125 Bari, Italy.

[2] Université Paris-Diderot, Institut de Physique du Globe de Paris, UMR CNRS 7154, 1 rue Jussieu, 75238-Paris cedex 05, France.

[3] Faculty of Science, Technology, Engineering & Mathematics (STEM), The Open University, Walton Hall, Milton Keynes, MK7 6AA, United Kingdom.

[4] CNR-IGG, Via G. Moruzzi 1, 56124 Pisa, Italy.

* Corresponding author: caterina.bianco@uniba.it.

Abstract

Evidence of high-P blueschist-facies metamorphism was found in metabasites embedded in calcschists of the Eastern Elba Island (Northern Apennines, Italy). The immobile trace elements (REEs and HFSEs) of the metabasites indicate an affinity with T-MORBs. The minerals are heterogeneously distributed in the rock, defining mafic and Ca-Al-rich microdomains inherited respectively from the pyroxene- and plagioclase-rich zones of the original doleritic rock. The highest pressure paragenesis consisted of lawsonite, aegirine-omphacite, glaucophane and chlorite. Lawsonite was replaced by pseudomorphs 0.1 mm in size, with the shape of rhombic prisms and consisting of clinozoisite with inclusions of muscovite ± albite ± quartz. The inclusions are preferentially orientated parallel to one of the diagonals of the basal rhombic sections, indicating that the two diagonals were not crystallographically equivalent, implying that the protocrystals were orthorhombic prisms with {110} faces, which is indeed the case of lawsonite. The compositions of white mica and epidote are different in the pseudomorphs (muscovite and Fe^{3+}-poor clinozoisite) and in the matrix (phengite and Fe^{3+}-rich epidote), indicating that the protomineral was devoid of Mg and Fe, which still points to lawsonite. Thermodynamic modelling, using the THERMOCALC software and dataset, suggests that metabasites experienced a clockwise P-T path from the lawsonite-blueschist subfacies to the epidote-blueschist subfacies, down to greenschist facies. The estimated peak pressure conditions are $P \geq 1.6$

GPa and 450 < T < 500°C. Glaucophane grew mainly during the lawsonite-to-epidote transition and is dated at 19.8 ± 1.4 Ma by the $^{40}Ar/^{39}Ar$ method. This evolution is interpreted in terms (i) injection of basic magmas in carbonated and pelitic sediments (early Oligocene), (ii) subduction (Oligocene), (iii) collision (early Miocene: 19.8 ± 1.4 Ma), (iv) exhumation and granite intrusion (Upper Miocene) favoured by extensional tectonics. The attribution of these rocks to the Ligurian palaeo-ocean domain is here rejected; they could rather be attributed to the western margin of the Adria plate. The eastern part of Elba Island belongs to a blueschist-facies belt that extends from Gorgona Island in the northwest to Argentario and Giglio Island in the southeast, so much of the conclusions of this study can be extended to the whole of this belt.

Keywords

HP-LT metamorphism, blueschist facies, Northern Apennines, Elba Island, P-T pseudosection, $^{40}Ar/^{39}Ar$ geochronology.

1. Introduction

In the Northern Tyrrhenian Sea (Fig. 1), from Corsica to Tuscany, high-pressure (HP) and low-temperature (LT) metamorphic conditions have been widely recognized in metasediments and metabasites (e.g. Rossetti et al., 2002). According to several authors (Carmignani et al., 1994; Rossetti et al., 2015 and references therein), these HP-LT imprints are related to the subduction and subsequent thickening of the Adria crust during the Northern Apennines orogeny, subsequently dismantled by extensional tectonics, active since early-middle Miocene (Brogi and Liotta, 2008; Molli, 2008; Barchi, 2010).

From Corsica to Tuscany, peak pressures and metamorphic ages (Fig. 1a) tend to decrease eastwards, from 2 to ~1 GPa (Rossetti et al., 2002) and from Palaeocene-Eocene to early Miocene (Brunet et al., 2000), because of the progressive burial towards the east during the formation of a thick accretionary complex, and the along-strike variations of the subduction system through time (Molli, 2008; Brunet et al., 2000). The most common blueschist-facies index minerals are the carpholite-chloritoid pair and phengite in the metasediments, and glaucophane, lawsonite and jadeite-rich pyroxene in the metabasites, yielding estimated P-T values ranging between 0.6 and 1.5 GPa at 275–450°C (Fig. 1a).

Although structurally close to the Adria-Europe suture zone, the island of Elba has been considered as a sector of the orogeny affected only by low-P (LP) metamorphism. However, evidence for blueschist-facies HP-LT metamorphism has been found near Rio Marina (eastern Elba) in metasediments (Pandeli et al.,

2001) and metabasites embedded in calcschists (Bianco et al., 2015). Achiardi (1896) has also described so-called eclogites in central Elba, but these are actually rodingites embedded within serpentinite. The purpose of this article is (i) to describe the HP-LT metamorphic rocks found near Rio Marina, (ii) to reconstruct their P-T-t path by thermodynamic modelling, and (iii) to date this HP-LT metamorphism. The aim is to decipher and better constrain the role of the Tuscan Archipelago in the collisional evolution of the Northern Apennines.

2. Geological setting

2.1. Northern Apennines

The northern Apennines originated from the convergence and collision between the Adria microplate and the Sardinian-Corsican massif (Cretaceous-early Miocene), producing the eastward stacking of oceanic and continental tectonic units (Fig. 1b; e.g. Boccaletti et al., 1971; Molli, 2008), which experienced blueschist- to greenschist-facies metamorphism (Fig. 1a; e.g. Gillet and Goffé, 1988; Carmignani and Kligfield, 1990; Fournier et al., 1991; Carmignani et al., 1994; Giorgetti et al., 1998; Brunet et al., 2000; Rossetti et al., 2002; Molli, 2008; Brogi and Giorgetti, 2012). In particular, metamorphic units in southern Tuscany experienced P-T conditions of 0.6–1.4 GPa and 350–450°C for the metasediments, and 0.7–0.8 GPa and 340–350°C for metabasites (Kligfield et al., 1986; Giorgetti et al., 1998; Brogi and Giorgetti, 2012). Similarly, the metasediments of the Tuscan Archipelago (Gorgona, Elba and Giglio islands) and Argentario Promontory have equilibrated at 1.0–1.5 GPa and $T \leq 350$°C, while metabasites were formed at 0.6–1.2 GPa and 330–450°C (Fig. 1a; Theye et al., 1997; Rossetti et al., 2001; Bianco et al., 2015 and references therein). Since the early-middle Miocene, extensional tectonics, migrating eastward, affected the inner part of Northern Apennines (Carmignani et al., 1994; Molli, 2008; Barchi, 2010; Rossetti et al., 2015) and was accompanied by exhumation and widespread magmatism (Carmignani et al., 2004; Brogi, 2008; Molli, 2008).

This general framework has been recognized on the Elba Island, where seven main units (Bianco et al., 2015), belonging to continental or oceanic crustal environments (Bortolotti et al., 2001), have been described (Figs. 2 and 3). The stacking of oceanic and continental units, as well as their duplication by post-stacking out-of-sequence thrusts (Keller and Pialli, 1990; Pertusati et al., 1993), can be related to the ongoing compression during the convergence between Adria and Sardinia-Corsica. During Miocene, extensional

79 tectonics produced low angle normal faults (Fig. 2), coeval and subsequent to the emplacement of the Monte
80 Capanne monzogranite in the west (~7.0 Ma: Westerman et al., 2004) and that of Porto Azzurro in the east
81 (~6 Ma: Maineri et al., 2003; Gagnevin et al., 2011), favouring the uplift and exhumation of the plutons and
82 their host rocks (Caggianelli et al. 2014; Liotta et al., 2015, with ref. therein). Magma emplacement, cooling
83 and hydrothermalism produced thermo-metamorphic aureoles, with LP mineral assemblages, overprinting
84 older metamorphic paragenesis related to the collisional event (e.g. Duranti et al., 1992; Pertusati et al.,
85 1993; Caggianelli et al., 2018).

2.2. The succession hosting the metabasite

86 The studied metabasite belongs to the Continental Unit 2 of Bianco et al. (2015), which is well exposed
87 near Rio Marina on the east coast of Elba Island (Fig. 2; "Phy" in Fig. 4). This unit is overthrust by a
88 serpentinite slice (i.e. Oceanic Unit 1 of Bianco et al., 2015; Figs. 2-4), and overlays the Mesozoic
89 metacarbonate succession partially involved in the Neogene metasomatism (Fig. 3). The total observable
90 thickness of this succession is estimated at about 200 m, although its top is interrupted by the tectonic
91 contact with the overlapping serpentinite slice (Figs. 2-3b).

92 The lowermost part of the unit (i.e. Porticciolo subunit of Pandeli et al., 2001; c in Fig. 3b), about 40 m
93 thick, consists of calcschist and marble, with cm-thick layers of gray-green phyllite (Calcschist lithofacies in
94 Bortolotti et al., 2015), where the studied metabasite lenses with HP metamorphic assemblage were
95 recognized (Bianco et al., 2015; d in Fig. 3b). The upper 20 meters include massive black phyllite passing to
96 dark gray marble and calcschist, often interspersed with black to green phyllite.

97 The upper part of the unit (i.e. Acquadolce Fm in Jacobs et al., 2018) is dominantly characterized by
98 metasandstone (a in Fig. 3b) with a thickness of up to 20 m. Minor cm- to dm-thick metasandstone levels
99 occur as precursor in the underlying 50 m dominated by phyllite (b in Fig. 3b). Detrital zircon from the
100 metasandstone levels has recently been studied by Jacobs et al. (2018). They interpreted it as derived from
101 the volcanic arc, active during subduction and deposited in the foredeep of the Apennine orogen. Zircon
102 dating by LA-ICP-MS and SHRIMP yielded a most populated age at 31.6 ± 0.5 Ma.

3. Petrography

Five representative samples of metabasites were selected for this study (RMT3A, RMT4A, RMT5B, RMT7A and RMT19). They were taken at the Rio Marina harbour (Figs. 2, 4-5), at the foot of the tower (N42°48'54.9"–E10°25'53.3"), where the carbonate-terrigenous part of "Continental Unit 2" is well exposed (Figs. 4-5). Here, marble and calcschist contain several lenses of metabasite, affected by a widespread boudinage at different scales.

The structures of the host calcschists are characterized by an S-C fabric, isoclinal folds associated with axial plane foliation, and NW-SE-trending stretching lineation, clearly underlined by calcite and quartz elongation (Fig. 6a). Intense deformation is also highlighted by widespread core-and-mantle microstructures (Fig. 6b), affecting both calcite and quartz, thus indicating progressive recrystallization processes. The mineral assemblage, oriented along the main foliation, consists of Cal + Dol + Qtz + Bt + Ms + Chl ± Ti-Fe oxides ± Ab ± Ap ± Ep (abbreviations after Kretz, 1983).

The mineralogical assemblage of the metabasite samples includes Gln + Cpx + Ep + Chl + Ab + Ms ± An ± Act ± Cal ± Qtz ± Ttn ± Rt ± Ap ± Mag. These rocks are fine-grained and display a mylonitic fabric characterized by clinopyroxene porphyroclasts dispersed in a matrix composed mainly of Ep + Gln + Chl + Ab + Ttn (Fig. 6c–g). Most of the glaucophane is syn-kinematic, as it concentrates in the strain shadows of pyroxene porphyroclasts, wrapping and forming stretched coronas around these (Fig. 6c, d). As a result, the rock exhibits strong heterogeneity, inherited in part from the magmatic protolith (Section 7.1.1), with three main types of microdomains:

(a) Mafic microdomains consist mainly of clinopyroxene porphyroclasts (Fig. 6c), a few millimetres across, which can be derived from magmatic pyroxene crystals. They are stretched and fractured, with glaucophane and chlorite filling the voids resulting from their parting (Fig. 7e, f). These porphyroclasts have been partially to completely replaced by fine-grained symplectites composed of Di + Qtz + Chl ± Ab ± Ttn (Fig. 7).

(b) The Ca- and Al-rich microdomains of the matrix are mainly composed of epidote, calcite, titanite, glaucophane, micas, actinolite and albite (Fig. 7c-f). Epidote forms subhedral mm-sized grains, in which the back-scattered-electron (BSE) images commonly reveal a chemical zonation mainly related to variations in the Fe^{3+} content. An interesting microstructure has been recognized in the RMT3A sample, where epidote single crystals contain inclusions of titanite, apatite, euhedral glaucophane with clearly recognizable basal

sections (Figs. 6g, 8a-d), and especially poly-mineral inclusions of about 100 μm in size, which display regular prismatic or rhombic forms and consist of clinozoisite + muscovite ± albite ± quartz ± calcite (Fig. 8). In other samples, these prismatic clinozoisite-bearing aggregates are embedded in chlorite and show only a thin epidote overgrowth (Fig. 7d, bottom). Because of their prismatic shapes, they are considered pseudomorphs after lawsonite (Section 7.1.2). Albite is common in the matrix, whereas, in a few samples, anorthite is also present in the form of tiny crystals (Fig. 6e). Ilmenite, titanite, phengite, apatite and rutile, locally included in titanite crystals (Fig. 6f), are common accessory minerals of the matrix.

(c) Glaucophane, as well as minor actinolite, is well developed in the strain shadows of pyroxene porphyroclasts (Figs. 6c, 7a-b), and often wraps around them, forming very irregular coronas between the above mafic and Ca-Al-rich microdomains (Fig. 7b-c). Glaucophane crystals are generally elongated with no discernible optical zonation, although a slight compositional zoning can be detected with the microprobe (Section 4.2) and BSE images showing locally a brighter actinolitic rim when in contact with albite.

Finally, magnetite microcrystals are sometimes clustered and may represent pseudomorphs after a previous Fe-rich magmatic mineral (e.g. Fig. 8a and c, top left). Calcite is quite common; it frequently forms small, late veins that may intersect the main foliation (Fig. 7e-f bottom).

4. Chemistry

In what follows, we report data relating to the chemical study of the samples. For the sake of clarity, this section is divided into two parts dealing with bulk-rock and with mineral chemistry.

4.1. Major and trace elements chemistry

Bulk-rock analyses were performed on the metabasites, in particular on the sample RMT3A, which is the most significant in terms of microstructures. The analyses for the major elements were carried out at the University of Bari, using Panalytical AXIOS-Advanced spectroscopy with X-ray tube SST-mAX (Super Sharp end-window Tube). The results for RMT3A are reported in Table 1, while the analyses of three other samples are given by Bianco et al. (2015).

The sample RMT3A shows a low content of SiO_2 (42.54 wt%) and K_2O (0.55 wt%), with a high content of MgO and FeO (X_{Mg} = Mg/[Mg+Fe+Mn] = 0.710); Na_2O is also relatively high (2.75 wt%). The normative mineral calculation, carried out via the CIPW norm, makes it possible to assess the mineralogical

composition of the magmatic protolith, provided that the chemical composition of the rock has not been modified during metamorphism. The normative quantities of minerals for the RMT3A sample, converted to volume percentages, correspond to an undersaturated magmatic rock (setting Fe^{3+} at 0.1 × Fe_{total}) with: 59.4 vol% plagioclase ($Or_7Ab_{30}An_{64}$); 21.9% olivine; 10.1% clinopyroxene; 6.2% nepheline; 1.3% ilmenite; 0.8% magnetite; 0.3% apatite. The average of four metabasite analyses (Bianco et al., 2015) gives similar results: 59.6 vol% plagioclase ($Or_8Ab_{36}An_{56}$); 19.1% olivine; 14.0% clinopyroxene; 4.9% nepheline; 1.3% ilmenite; 0.9% magnetite; 0.3% apatite.

Analyses of trace elements, performed at Actlabs® laboratories by ICP-MS, were carried out on four samples (Tab. 2) to better constrain the geochemical signature of the protolith. The chondrite-normalized REE patterns (Fig. 9a) show a slight LREE enrichment, up to 25× for La, with high ratios of LREE/HREE (e.g. $[Ce/Yb]_N$ = 1.81–2.02). The positive Eu-anomaly (average Eu/Eu^* = 1.11) indicates a plagioclase accumulation or segregation. These patterns are clearly intermediate between those of N-MORBs, depleted in LREE, and E-MORBs, strongly enriched in LREE. In addition, excluding the large-ion lithophile elements (LILE: e.g. K, Rb, Cs), because of their mobility during metamorphism, and the alkaline earth elements (Sr, Ba), which may be involved in diffusion processes from the neighbouring calcschists, the trace elements show contents between 10× and 4× those of the primitive mantle. All these characteristics are similar to those of T-MORB (transition basalt between N-MORB and E-MORB; Figs. 9–10). In addition, the ratios between high-field-strength elements (HFSE) are similar to those of T- and E-MORB (Geshi et al., 2007; Sun and McDonough, 1989; Liu et al., 2015; Karsten et al., 1990), as shown by the Y/Nb (from 3.603 to 4.098), Zr/Nb (15.00–18.05), La/Sm (1.933–2.194), and Ti/Y (289.3–367.5) ratios. Another important feature is the higher Zr/Y ratio (3.98–4.16: Fig. 10b) compared to a pure mantle source (Zr/Y = 2.64; Sun and McDonough, 1989), which suggests crustal contamination.

4.2. Mineral chemistry

The electron microprobe analyses were carried out using a Cameca SX-100 electron microprobe (Camparis laboratory, Paris, France). Analytical conditions were 10 nA beam current and 15 kV acceleration voltage. Representative mineral analyses of the four studied samples are presented in Tables 3 and SM1–SM3 in the supplementary materials. The structural formulas are calculated on the basis of quantities of anions O and OH, chosen according to the mineral group: epidotes: $O_{12}(F,OH)_1$ and Fe^{3+} = Fe_{total}; micas:

$O_{20}(OH,F)_4$, Fe^{3+} = 0; chlorites: $O_{20}(OH)_{16}$, Fe^{3+} = 0; feldspars: O_8, Fe^{3+} = Fe_{total}; pyroxenes: O_6, Fe^{3+} value corresponding to 4 cations; amphiboles: procedure of Hawthone et al. (2012), giving a range of Fe^{3+} values for which the cation distribution in the T, C, B and A sites is correct; for glaucophane, the formula with Na_A = 0 is preferred if $0 < Fe^{3+} < Fe_{total}$. Mineral abbreviations are from Kretz (1983).

Clinopyroxenes are mainly aegirine-augite/omphacite and their composition is highly variable with X_{Jd} ranging from 0.292 down to 0.122 (Fig. 11a). This variation does not correspond to a clear zonation of the crystals, but more to a chemical heterogeneity on a very small scale which could correspond to exsolution, perhaps related to the existence of a LT solvus between omphacite/aegirine and augite, but also to a partial decomposition of aegirine/omphacite into chlorite, albite and Jd-poor clinopyroxene (Section 3). The two groups around $Jd_{22}Ae_{25}Aug_{53}$ and $Jd_9Ae_{19}Aug_{72}$ in Figure 11a correspond to the primary Jd-rich and secondary Jd-poor pyroxenes, respectively.

Amphiboles are Na-amphibole and less abundant actinolite, often located within the clinopyroxene strain shadows. Na-amphibole is almost pure glaucophane (Fig. 11b) according to the nomenclature of Hawthorne et al. (2012), with X_{Gln} ranging from 0.69 to 0.99 (calculated as $Al^{VI}/[Fe^{3+}+Al^{VI}]$). A slight zonation is perceptible in the matrix crystals, with the reverse glaucophanitic substitution (i.e. Al_{-1} [Mg, $Fe^{2+}]_{+1}$ Ca_{+1} Na_{-1}) operating from core to rim.

The analyses reveal two types of ***epidote***: (i) some Fe^{3+}-rich epidote with an X_{Fe3+} ratio, calculated as $Fe^{3+}/(Fe^{3+}+Al)$, ranging from 0.217 to 0.359, which corresponds to a molar fraction of pistacite varying from 0.78 to 0.92 (X_{ps} = Fe/[Al-2+Fe]); (ii) clinozoisite with a lower X_{Fe3+}, between 0.025 and 0.176, which corresponds to an X_{ps} interval of 0.31 to 0.40. Fe^{3+}-rich epidote is abundant in the matrix; it contains microcrystalline inclusions of the Fe^{3+}-poor clinozoisite, which, together with muscovite, albite, calcite and quartz, forms pseudomorphs that we interpret as having replaced euhedral prismatic lawsonite (Fig. 8; Section 7.1.2).

The analyses reveal two different types of ***white micas***: (i) fine-grained muscovite was detected in the clinozoisite-rich pseudomorphs described above; its analyses show a low Mg content, of about 0.030 atoms per formula unit (a.p.f.u.); (ii) in contrast, phengite found in the matrix has an Mg content up to 0.073 a.p.f.u.

Plagioclase has an albitic composition (Ab_{93} on average), both in the matrix and in the clinozoisite-rich pseudomorphs. In two samples (RMT19, RMT4A), small crystals of anorthite-rich plagioclase were also found ($An_{79–99}$).

Chlorite is rich in Fe and Mg, with X_{Mg} around 0.93. It is classified as ripidolite according to the nomenclature of Hey (1954). ***Apatite*** is fluoroapatite with F ≈ 2.9 wt%. ***Titanite*** is common and often contains relicts of ***rutile*** (Fig. 6f). ***Magnetite*** has also been observed.

5. Geochronology: $^{40}Ar/^{39}Ar$ dating

Glaucophane from sample RMT7a was dated by $^{40}Ar/^{39}Ar$ using step heating, with a MAP215-50 mass spectrometer and 1059 nm CSI fibre laser. The separated mineral was irradiated for 117 hours at the McMaster Nuclear Reactor, Canada, along with the biotite mineral standard GA1550 (99.738 ± 0.104 Ma: Renne et al., 2010). Data were corrected for mass discrimination (using a value for $^{40}Ar/^{36}Ar$ of 283, determined from a known composition calibration gas), and for system blanks measured before and after 2 analyses. Corrections for ^{37}Ar and ^{39}Ar decay since irradiation were applied and the following correction factors used for neutron-induced interference reaction: $(^{39}Ar/^{37}Ar)_{Ca}$ = 0.00065 ± 0.00000325, $(^{36}Ar/^{37}Ar)_{Ca}$ = 0.00026 ± 0.000001325, and $(^{40}Ar/^{39}Ar)_{K}$ = 0.0085 ± 0.0000425, based on analyses of Ca and K salts. Ages were calculated using the atmospheric $^{40}Ar/^{36}Ar$ ratio of 298.56 (Lee et al., 2006), and decay constants of Renne et al. (2011). This is reported at 2σ level and includes a 0.5% error on the J value.

An age of 19.8 ± 1.4 Ma is then calculated from the inverse isochron analysis of the step-heating data. This inverse isochron (Fig. 12) computes an initial $^{40}Ar/^{36}Ar$ within error of atmospheric ratio (285 ± 12), suggesting that it is not affected by argon excess. Although no plateau age can be calculated from the release spectra, the apparent ages fall between 18 and 20 Ma, similar to the isochron age, suggesting that this is the best estimate for the age of the glaucophane.

6. P-T modelling

P-T pseudosections are used to model the stability of mineral assemblages in the P-T space, using chemical bulk compositions that closely approximate the actual rock. We constructed such a P-T pseudosection, using the THERMOCALC software (Powell and Holland, 1988; version 3.33 updated in June 2011) and the updated ds55 version of the thermodynamic dataset from Holland and Powell (2011).

The P-T pseudosection of Figure 13 is based on the bulk composition of the RMT3A metabasite (Tab. 1), converted to molar percentages. The P_2O_5 component was subtracted by projection onto the P_2O_3-free subspace from the composition of apatite, not taken into account in the modelling. The minor component K_2O has been neglected because it mainly enters the amphibole compositions whereas the composition-activity model used for these amphiboles does not take it into account. MnO, another minor component also incorporated into amphiboles and chlorite, has been added to FeO for the same reason. The amount of O (i.e. Fe^{3+}) was estimated from the structural formulas and molar amounts of peak minerals, estimated by the least-square method (see Godard, 2009); it must be borne in mind that this value could have changed during metamorphism. H_2O is considered to be in excess, which seems reasonable given the abundance of hydrated minerals and the high LOI value (Tab. 1). Therefore, the modelling was carried out in the NCFMASHTO system, using the following bulk composition (mol%): $(SiO_2)_{47.73}$ $(Al_2O_3)_{11.17}$ $(CaO)_{10.93}$ $(MgO)_{18.17}$ $(FeO)_{7.43}$ $(Na_2O)_{2.99}$ $(TiO_2)_{0.76}$ $O_{0.82}$.

The activity-composition models used for solid solutions are: Green et al. (2007), revised by Diener and Powell (2012), for omphacitic clinopyroxenes; Holland et al. (1998) for chlorite; White et al. (2007) for garnet; Holland and Powell (1998) for epidote; Holland and Powell (2003) for plagioclase; Diener et al. (2007), revised by Diener and Powell (2012), for hornblende, actinolite and glaucophane, which can be co-stable. Lawsonite, rutile, titanite and quartz are considered pure phases.

It should be emphasized here that a P-T pseudosection must in principle apply to a homogeneous system, which is not really the case for the rocks studied, where various microdomains, presumably inherited from the magmatic protolith, have partially survived deformation and diffusion. The same mineral can be highly zoned and its composition can vary significantly from one microdomain to another (Section 4.2). Normally, isopleths are used to explain changes in the mineral composition and to better constrain the P-T path of the rock studied. In our case, however, the observed heterogeneity makes this approach difficult. The X_{Fe2+} and X_{Fe3+} ratios of the zoned minerals are highly variable and, moreover, subject to great uncertainties related to the stoichiometric estimation of Fe^{3+}. The isopleths corresponding to these ratios are therefore dispersed in wide T intervals of the pseudosection and thus give little useful constraints. Two sets of isopleths have nevertheless been retained because they can provide relatively reliable information; they are based on the

composition of clinopyroxene (X_{Jd+Ae} = Na/Na+Ca: blue curves in Fig. 13) and that of glaucophane (Z_{Gln} = Na fraction in B site, considering Na_A negligible: red curves in Fig. 13).

The pseudosection (Fig. 14) is composed of 2 to 7th variant P-T fields, whose corresponding mineral assemblages are indicated by abbreviations (Kretz, 1983), those in parentheses being in very low modal quantity (<1 vol%). The information derived from this pseudosection is presented in the course of the discussion below.

7. Discussion

7.1. Petrological evolution of the metabasites

We focus here on the evolution of the studied metabasites (i.e. protolith, metamorphic evolution, dating). The microstructures observed, as well as the mineral composition and zoning, reveal several metamorphic stages, which we detail here.

7.1.1. Protolith

The protolith was a magmatic rock, with a grainy texture as evidenced by the preservation of mafic and Ca-Al-rich microdomains that would represent the former magmatic pyroxene and plagioclase, respectively. The size of the pyroxene porphyroclasts, which reach a few millimetres, gives an appreciation of the grain size of the protolith.

The CIPW norm suggests that the protolith was a basic rock undersaturated in silica, resulting in the presence of normative olivine and nepheline (Section 4.1). It is likely, however, that the contents of Si and other major elements have been modified during metamorphism, when the rock was boudinaged within calcschists of very different composition. To better constrain the geochemical signature of the protolith, it is therefore preferable to consider only the immobile trace elements, like REEs and HFSEs. These imply that the protolith had a composition of T-MORB (Section 4.1). The positive Eu/Eu* anomaly also indicates either plagioclase accumulation in a magmatic chamber or plagioclase segregation by flowage differentiation. Based on field observations, in particular the structural framework, the reduced thickness of the lenses and their interbedding with calcschists (Fig. 5), the study metabasites can be interpreted as former dolerite sills and/or dykes.

7.1.2. Lawsonite blueschist metamorphic stage

As previously described (Section 3), the epidote crystals present in the matrix of sample RMT3A contain poly-mineral inclusions, consisting of clinozoisite + muscovite ± albite ± calcite ± quartz and showing regular rectangular and rhombic shapes (Fig. 8); in other samples, the same poly-mineral aggregates are included in chlorite (Fig. 7d bottom). Such a microstructure is commonly interpreted as pseudomorphs after lawsonite (e.g. Félix and Fransolet, 1972; Tsujimori et al., 2006; Groppo and Castelli, 2010; Angiboust et al., 2012; López-Carmona et al., 2014; Orozbaev et al., 2015). In our case, several points corroborate this interpretation:

(a)- These prismatic inclusions have a random orientation relative to the host single crystal of epidote (Fig. 9). They cannot therefore be interpreted as inherited cores or exsolution structures of the latter, and are thus necessarily pseudomorphs.

(b)- The outline of these pseudomorphs appears sharp in the BSE images (Fig. 8), because the Fe^{3+}-poor clinozoisite that constitutes them (medium gray) contrasts with the host Fe^{3+}-rich epidote (light gray). The composition of the (Mg, Fe)-free muscovite included in the pseudomorphs also contrasts with that of Mg-rich phengite in the matrix (Section 4.2). These compositional differences indicate that the protomineral did not contain Fe and Mg, corroborating that it was lawsonite.

(c)- The apparent shapes of these pseudomorphs grade between rectangles (2 in Fig. 8b, e) and rhombs (1 in Fig. 8b, e), which respectively correspond to longitudinal and basal sections of rhombic prisms. The inclusions of muscovite and albite are parallel to the long side of the rectangular longitudinal sections, thus to the prism elongation, whereas they are preferentially oriented parallel to one of the diagonals of the basal rhombic sections (see red lines in Fig. 8b, e), which means that the two diagonals were not crystallographically equivalent. This strongly suggests that the protocrystals were orthorhombic prisms with {110} faces, which is a common habit of lawsonite.

In addition to the pseudomorphs after lawsonite, the single crystals of epidote contain microinclusions of euhedral glaucophane, apatite and titanite with scarce relicts of rutile (Fig. 8). Moreover, the same epidote crystals show elongated sheet-like zones that appear brighter in BSE, being richer in Fe^{3+} (barely visible in Fig. 8d). Since these zones are positioned in the prolongation of chlorite sheets of the matrix, they resulted from the replacement of chlorite that occupied, probably with other minerals, the interstices between the

prisms of lawsonite and glaucophane. Thus, the first recognizable metamorphic paragenesis consisted of lawsonite, glaucophane, chlorite, apatite, titanite and/or rutile and possibly a little phengite in the Ca- and Al-rich microdomains after plagioclase, whereas the mafic microdomains after pyroxene were likely already transformed into omphacite/aegirine, as suggested by the pseudosection (see below). Clusters of iron oxides could be derived from another mineral, such as spinel or iddingsite, a Fe-rich and Si-poor form of olivine alteration.

This paragenesis, which predates epidote, must have been formed under the HP conditions of the lawsonite-blueschist subfacies (e.g. Evans, 1990). In the P-T pseudosection, the mineral assemblages with Chl + Lws + Gln + Omp ± Act + Rt/Ttn appear stable at high pressure, beyond a limit ranging from 1.2 GPa–400°C to 2.0 GPa–550°C (Fig. 13). Some elements, unfortunately not very accurate, make it possible to restrict these conditions: (i) the P-T conditions cannot have exceeded 2.0 GPa–550°C, since garnet, which was never observed in these rocks, should have appeared in such conditions; (ii) the presence of relict rutile within a few titanite crystals (Fig. 6f) suggests that rutile-bearing fields have been reached (i.e. "Chl (Act) Gln Omp Lws Rt" or "Chl Gln Omp Lws Rt" in Fig. 13); (iii) the isopleths Z_{Gln} applied to the early glaucophane enclosed within epidote (Z_{Gln} = 0.919 ± 0.027 [1σ]), despite the reservations about their reliability (Section 6), suggest temperatures around 460°C (Fig. 13). We can therefore retain the following conditions for this stage of metamorphism: 450 < T < 500°C; P > 1.6 GPa.

The pseudomorphs after lawsonite and crystals of glaucophane enclosed in the single crystals of epidote have no clear preferential orientation, being oriented randomly (Fig. 9), which suggests that the deformation was not intense at this stage.

7.1.3. Epidote blueschist stage

The breakdown of lawsonite into clinozoisite + muscovite ± albite ± calcite ± quartz cannot occur in a closed system. Indeed, it requires some interaction with other minerals present in the matrix (e.g. Orozbaev et al., 2015) and the mobility of alkalis. We have balanced a possible metamorphic reaction, assuming the mobility of alkalis and water:

1 Lws $[Si_2Al_2CaO_7(OH)_2.H_2O]$ + 0.083x K_2O + 0.050(1-x) Na_2O =

0.500 Czo $[Si_3Al_3Ca_2O_{12}(OH)_1]$ + 0.167x Ms $[Si_3Al_3K_1O_{11}(OH)_2]$ + 0.100(1-x) Ab $[NaAlSi_3O_8]$ + 0.200(1-x) Ky $[SiAl_2O_5]$ + (1.750 - 0.167x) H_2O, with $0 < x < 1$.

Such a theoretical reaction produces clinozoisite, muscovite and albite, as observed in the pseudomorphs, and could thus approach reality.

In addition to the replacement of lawsonite by clinozoisite, growth of epidote (pistacite) encompassing both lawsonite pseudomorphs and glaucophane crystals is observed in the Ca- and Al-rich microdomains (Fig. 8). This epidote is in equilibrium with ubiquitous glaucophane, which tends to concentrate in coronas between the Al-rich and mafic microdomains (Section 3), as its growth required the inputs of Al and Na from the Al-rich microdomains (i.e. the matrix) and those of Fe and Mg from the mafic microdomains (i.e. the pyroxene porphyroclasts).

The mineralogical assemblages observed at this metamorphic stage are typical of the epidote-blueschist subfacies (e.g. Evans, 1990). The P-T pseudosection of Figure 13 shows that the transition between the above lawsonite-bearing stage and this new epidote stage occurs in a narrow P-T strip, about 0.05-GPa wide between 1.1 GPa–400°C and 1.9 GPa–540°C, consisting of various multivariant P-T fields where lawsonite and epidote coexist. We calculated the modal quantities of the minerals, expressed in volume percentages, at two P-T points of the pseudosection (dots in Fig. 13), before and after the transition:
1.6 GPa, 475°C (vol%): 15.0 Gln + 0.6 Act + 24.9 Omp + 30.2 Chl + 28.6 Lws + 0.0 Ep + 0.7 Rt + 0.0 Tnt;
1.5 GPa, 480°C (vol%): 34.3 Gln + 2.0 Act + 4.9 Omp + 28.1 Chl + 0.0 Lws + 28.7 Ep + 0.0 Rt + 2.0 Tnt.

These results properly accounts for several petrological observations: (i) in the first place, the transformation of lawsonite into epidote; (ii) the replacement of rutile by titanite, the P-T fields where titanite is stable being wider after the transition than before (Fig. 13); and most importantly (iii) the growth of glaucophane (Gln), and incidentally actinolite (Act), at the expense of omphacitic pyroxene (Omp), thus explaining the presence of glaucophane around, as well as in the strain shadows and fractures of the pyroxene porphyroclasts (Fig. 7). However, the growth of glaucophane at the expense of pyroxene was not as complete as predicted by the model, since ideally the amount of pyroxene should have reduced down to ~4.9 vol% at this stage. This reflects a lack of equilibrium at the global level of the rock, as already emphasized.

The assemblage Chl + Gln + Act + Omp + Ep + Tnt corresponds to temperatures of about 450–520°C for a pressure that can range from 1.5 to 0.9 GPa without notable modification of the mineral paragenesis. The zonation of amphibole crystals, with a slight decrease in the glaucophane end-member from core to rim

(Section 4.2), suggests an evolution at decreasing P and/or increasing T. Applying the Z_{Gln} isopleths to the average compositions of the cores (Z_{Gln} = 0.900 ± 0.025 [1σ]) and rims (0.871 ± 0.049) of glaucophane crystals in the matrix confirms such an evolution up to around 520°C. Under these conditions, the model predicts an X_{Jd+Ae} ratio of 0.46 for the clinopyroxene, which is consistent with the composition observed (Fig. 11), if care is taken to exclude the values close to 0.30 that result from late albite exsolution.

The albitic plagioclase (Ab_{93}) that locally occurs in the pseudomorphs after lawsonite (Fig. 8) is stable only at pressures lower than the dashed curve of Figure 13, corresponding to the equilibrium Ab_{93} = Jd_{100} + Qtz, and hence at pressures below the lawsonite-epidote transition. It has to be admitted that lawsonite remained metastable for a certain time during decompression or, better, that albite developed secondarily from an Na-rich HP mineral like paragonite, common in such pseudomorphs (e.g. Félix and Fransolet, 1972; Groppo and Castelli, 2010; López-Carmona et al., 2014; Orozbaev et al., 2015).

Since a large part of glaucophane has developed and/or deformed at this stage, the dating at 19.8 ± 1.4 Ma (Section 5) is likely to be related to it. Moreover, since glaucophane developed in fractures and strain shadows of pyroxene porphyroclasts, most of the deformation probably occurred during this episode.

7.1.4. Greenschist-facies retrogression

The retrograde evolution is documented by the following features: (i) thin symplectites replacing omphacite (Fig. 7), as a consequence of the reaction Omp → Di + Chl + Qtz + Ab; (ii) the general development of albite (Ab_{93}) in the matrix (Fig. 9); (iii) the transformation of glaucophane into chlorite and calcic amphibole, particularly actinolite, on its borders and along fractures (Fig. 7).

This stage is characterized by Ep + Act + Ab + Chl + Di + Ttn as the main paragenesis, and thus indicates retrogression in greenschist-facies conditions. The pseudosection of Figure 13 indicates that, while glaucophane disappears, plagioclase and calcic amphiboles appear around 470–510°C, at P < 0.9 GPa. Under these conditions, the plagioclase predicted by the model (Ab_{92}) has a composition close to that observed (Ab_{93}: Section 4).

7.1.5. Late high-temperature imprint

The mm-sized crystals of anorthite observed in the matrix of a few metabasite samples (Fig. 6e) may have replaced some former epidote, which is quite common (e.g. Holdaway, 1972). Whatever its origin, this

anorthite suggests a late increase of temperature, probably due to the emplacement at 6.53 Ma of the Porto Azzurro granite pluton (Gagnevin et al., 2011) at shallow crustal level, as testified by the thermobarometric studies on the metamorphic aureole (0.2 GPa at 300–600°C: Pertusati et al., 1993; <0.2 GPa at 550–600°C: Musumeci and Vaselli, 2012; 6.5 ± 0.9 km at 630°C: Caggianelli et al., 2018).

7.2. Geodynamic implications

The study of the metabasites and calcschists leads to the following considerations:

(a) Despite probable chemical exchanges with the host calcschists, the immobile elements of the metabasites reveal an affinity with T-MORBs (Section 4.1). Moreover, calcschists with interbedded metabasites, together with serpentinites at their top and radiolarites at their base (Fig. 3) appear to be a kind of "Steinmann trinity" exhibiting many features of ophiolites. As already suggested by Duranti et al. (1992), Pertusati et al. (1993), Bortolotti et al. (2001) and Pandeli et al. (2001), these rocks could have belonged to the lithosphere of the Piedmont-Ligurian palaeo-ocean, which disappeared by subduction during Cretaceous-Eocene time (Boccaletti et al., 1971; Carosi and Montomoli, 2002; Molli, 2008). However, this hypothesis is hampered by the fact that the radiolarites are in succession with carbonatic platform rocks (Fig. 3), and by the dating of the neighbouring metasediments, which contain early Oligocene detrital zircons (31.6 ± 0.5 Ma: Jacobs et al., 2018; see above). The metabasite protolith, likely a micrograbbro or dolerite with T-MORB affinity (Section 7.1.1), may also have belonged to an atypical oceanic crust, such as a back-arc basin. This hypothesis is however poorly compatible with the Oligocene age of the detrital zircons in the metasediments, since subduction was already affecting the Adria plate during Oligocene, making it hardly compatible with a back-arc basin on the Adria margin (see Molli, 2008 for a review). Alternatively, the study rocks could be mafic bodies deriving from a mantle magma injected into the thinned Adria continental crust, as suggested by its crustal contamination (Fig. 10c). Accepting this latter view, the studied calcschists and metabasites could represent the lower part of the Scaglia Toscana Fm, deposited since late Cretaceous in the continental Tuscan Domain (Canuti et al., 1965; Kälin et al., 1979; Fazzuoli et al., 1996; Bambini et al., 2009).

(b) Metabasites have undergone HP-LT blueschist-facies metamorphism, as evidenced by the presence of omphacite, glaucophane and especially pseudomorphs after lawsonite (Sections 3 and 7.1.2). Thermodynamic modelling indicates conditions of more than 1.6 GPa and 450–500°C at maximum depth (Section 7.1.2), corresponding to a gradient of ~280°C/GPa (i.e. ~8°C/km) typical of subduction zones.

(c) The glaucophane dating yields an age of 19.8 ± 1.4 Ma ($^{40}Ar/^{39}Ar$ method: Section 5). Most of this glaucophane is syn-kinematic; pseudosection modelling indicates that much of it formed after the pressure peak during the lawsonite-epidote transition (Section 7.1.3). The glaucophane age is in good agreement with the $^{40}Ar/^{39}Ar$ dating carried out on syn-kinematic phengite defining the main schistosity of neighbouring calcschists (19.68 ± 0.15 Ma: Deino et al., 1992). This early Miocene episode should be ascribed to collision, as it followed subduction, preceded exhumation and was coeval with the main phase of deformation (Section 7.1.3). Early Miocene ages for the metamorphic event are also reported in Brunet et al. (2000) on the mainland close to Elba Island.

(d) The metabasites recorded a retrograde evolution, without significant deformation, under greenschist-facies conditions, and then underwent a LP heating episode attributable to the intrusion of the Porto Azzurro monzogranite. The exhumation corresponding to the retrograde evolution is Miocene, being consecutive to the collision (~20 Ma: see supra) and preceding the monzogranite intrusion (~6 Ma: Section 2.1).

Whether the study rocks belonged to an atypical oceanic lithosphere, whether they were injected into the thinned continental crust of Adria, or whether they belonged to the Cretaceous-Oligocene sub-Ligurian domain defined as being intermediate between the oceanic and continental domains (Cerrina-Feroni et al., 1991, Plesi et al., 1993), these seemingly divergent hypotheses basically reflect the same reality, namely the belonging of the study area to the margin of the Adria microplate, dragged into subduction during Oligocene, before reaching, at the beginning of the Miocene, HP conditions similar to those documented for Gorgona Island, Argentario Promontory and Giglio Island, where comparable lawsonite-bearing glaucophanites were also observed (Fig. 1; Section 2.1; e.g., Theye et al., 1997; Brunet et al., 2000; Rossetti et al., 2001). Further studies are however needed to investigate whether HP metamorphism affected the entire tectonic pile underneath the studied calcschists of the Elba Island.

8. Conclusions

The metabasites interbedded and stretched in calcschists at Rio Marina (Eastern Elba Island) possibly derived from dykes and/or sills with T-MORB geochemical affinity. The oldest preserved metamorphic paragenesis (Chl-Lws-Gln-Omp-Rt) reflects HP-LT metamorphic conditions of $P \geq 1.6$ GPa and 450–500°C, which correspond to subduction down to ca. 60 km depth (Fig. 14). Much of the glaucophane blastesis took place during a deformation episode at the lawsonite-epidote transition, within the blueschist facies; this

episode, attributed to the early Miocene by the dating of glaucophane (19.8 ± 1.4 Ma), is related to the collision. Gorgona Island, the eastern coast of Elba, the Argentario Promontory and Giglio Island contain serpentinites, metasediments and lawsonite-bearing glaucophanites (Fig. 1; Section 2.1). This NW-SE trend of about 150 km long thus seems to constitute a HP-LT metamorphic belt, largely masked by the Tyrrhenian Sea, and much of the conclusions of this study are likely applicable to the whole of this belt. With subsequent exhumation, favoured by extensional tectonics, the rocks were affected by retrograde metamorphism under greenschist-facies conditions. Finally, the intrusion of the Porto Azzurro pluton, during late Miocene, resulted in a weak imprint of LP thermal metamorphism, revealed by the local appearance of anorthite. In this frame, the eastern Elba Island continental units are attributed to the thinned margin of the Adria plate.

Acknowledgments

This research has received funding from the European Union's Seventh Framework Programme under grant agreement n° 608553 (project IMAGE).

Figure and Table Captions

Fig. 1 – Geology of the Northern Apennines

(a)- Structural sketch map of the inner Northern Apennines with metabasites (black circles) and metasediments (blue circles) affected by HP-LT metamorphism (after Bianco et al., 2015, modified). The P-T values and ages are from the bibliography (Section 2.1) and this study (n° 12). (b)- Tectonic units of Northern Apennines and related palaeogeographical domains (modified after Carmignani et al., 1994). From west to east, these domains are the Ligurian (i.e. oceanic), Sub-Ligurian and Tuscan (i.e. continental) domains (see text).

Fig. 2 – Geological sketch map of Elba Island

The tectonic units and their relationships are modified after Bianco et al. (2015). The Rio Marina study area is indicated by the black frame.

Fig. 3 – Tectono-stratigraphic pile of Elba Island.

(a)- Tectono-stratigraphic columns of the various tectonic units belonging to continental and oceanic environments; (b)- detail of the upper part of the "continental unit 2" (a-d: see text).

Fig. 4 – Geological map and cross-sections of the Rio Marina area

Fig. 5 – Sampling area in the Rio Marina harbour

(a)- Westward view of the sampling area; (b)- contact between metabasite and calcschist; (c, d)- metabasite laterally segmented at different scales within calcschists, which are foliated and deformed in tight isoclinal folds.

Fig. 6 – Microphotographs and BSE image of the studied metabasite and calcschists

Plane-polarized light (c, d, e), cross-polarized light (a, b, g) and BSE image (f); (a)- calcschist with elongated crystals of phengite, quartz and calcite; (b)- core and mantle microstructures in calcschist, indicating progressive recrystallization of calcite and quartz; (c)- fractured porphyroclast of clinopyroxene with glaucophane and actinolite in the strain shadows in metabasite; (d)- large glaucophane crystals in the matrix of metabasite; (e)- altered rock portion of metabasite with abundant titanite and anorthite testifying overprint of low-P thermal metamorphism; (f)- large titanite including rutile crystals in metabasite; (g)- epidote crystals in metabasite, enclosing glaucophane, albite and clinozoisite after lawsonite (see Fig. 9).

Fig. 7 – Pyroxene porphyroclasts within metabasite

Metabasite samples C19 (a, b, e, f) and RMT4A (c, d); red-green-blue (RGB) images (b, d, f) constructed from the first 3 main components obtained by PCA of chemical element maps and BSE images (a, c, e). (a, b)- A clinopyroxene porphyroclast, almost completely replaced by symplectites composed of Di + Chl + Qtz + Ab + Gln, is fractured and stretched in a matrix mainly composed of epidote and chlorite; glaucophane is concentrated in the strain shadow of the porphyroclast. (c, d)- Clinopyroxene partially transformed into symplectite (top) in a matrix with epidote, titanite and chlorite; glaucophane is concentrated in a corona between clinopyroxene and its matrix; clinozoisite crystals with prismatic forms (bottom) are pseudomorphs

after lawsonite (see text). (e, f)- Stretched and fractured clinopyroxene porphyroclast showing fractures filled with glaucophane and chlorite; the late fracture at bottom is filled with calcite.

Fig. 8 – Pseudomorphs after lawsonite in single crystals of epidote

Metabasite sample RMT3A; RGB images (c, f; see Fig. 7 for the technique) and BSE images (a, b, d, e). Rhombic basal sections (1) and rectangular longitudinal sections (2) of former lawsonite prisms replaced by clinozoisite, basal sections of glaucophane (3), apatite (4) and titanite (not visible) are all enclosed in single crystals of pistacite (5). The inclusions of muscovite, albite and calcite (dark gray) in pseudomorphs after lawsonite are preferentially oriented (red lines), suggesting an orthorhombic symmetry for the protomineral (see text). White mica is phengite in the matrix and muscovite in the pseudomorphs; glaucophane becomes actinolite along the fractures.

Fig. 9 – Spider diagrams for the Rio Marina metabasites

(a)- REE spider diagram normalized to chondrite (McDonough and Sun, 1995); (b)- Multi-elements spider diagram normalized to E-MORB (Sun and McDonough, 1989); (c)- REE spider diagram normalized to T-MORB (Klein, 2004).

Fig. 10 – Discriminant geochemical diagrams for the Rio Marina metabasites

Circles represent the studied metabasites; N-, T-, E-, P-MORB are normal, transitional, enriched and plume-type MORBs, respectively; OIB: Oceanic Island Basalt; OPB: Oceanic Plateau Basalt; (a)- Zr–Y diagram, with basalt fields by Amaral et al. (2011); (b)-Zr/Y-Nb/Y diagram, with fields from Ueda et al. (2000); (c)-Th/Yb-Nb/Yb diagram inferring contamination processes of primary basalts (Pearce, 2008).

Fig. 11 – Clinopyroxene and amphibole compositions in metabasite

(a)- Clinopyroxene compositions in the augite-jadeite-aegirine (Di+En+Fs+Hd, Jd, Ae) diagram; (b)- glaucophane analyses plotted in the diagram for Na-amphiboles (Hawthorne et al., 2012).

Fig. 12 – Glaucophane geochronology

(a)- Inverse isochron correlation plot (MWSD: Mean Weight Square Deviates); (b)- step-heating release spectra.

Fig. 13– P-T pseudosection of the Rio Marina metabasite

Modelling is based on the composition of sample RMT3A (see text). Fluid (pure H_2O) is assumed in excess. Stable assemblage fields are coloured by variance. Red and yellow lines are, respectively, the isopleths for the molar fraction of the glaucophane end-member in amphibole (Z_{Gln} = Na in M_4) and the jadeite-aegirine fraction in clinopyroxene (X_{Jd+Ae} = Na/Na+Ca). Dashed line is the stability limit for plagioclase Ab_{92} (see text). Black dots represent the P-T points, before and after the lawsonite-epidote transition, at which the modal quantities of the minerals are calculated (see text).

Fig. 14 – Geological evolution of Elba Island

The evolution is illustrated through sketched cross-sections related to specific steps of the P-T-t path deduced from this study. Main P-T boundaries are reported from the above pseudosection (Fig. 13); red dots: ages of glaucophane and the Porto Azzurro pluton intrusion; light green star: studied rocks from Rio Marina.

Table 1 – Bulk-rock composition of metabasite sample RMT3A

L.O.I.: loss on ignition.

Table 2 –Trace element composition of metabasite samples from Rio Marina.

Values are in µg/g (ppm).

Table 3 – Representative microprobe analyses for metabasite sample RMT3A

av(*n*): average of *n* analyses; *: total without H_2O, with FeO_{total} and subtraction of O≡F; **: glaucophane within epidote; ***: in the matrix; ****: in pseudomorphs after lawsonite.

Supplementary materials

Table SM1 – Representative microprobe analyses for metabasite sample C19

552 Av(n): average of n analyses.

553 Table SM2 – Representative microprobe analyses for metabasite sample RMT4A

554 Av(n): average of n analyses.

555 Table SM3 – Representative microprobe analyses for metabasite samples RMT5B and RMT7A

556 Av(n): average of n analyses.

References

557 Achiardi, G. D', 1896. Il granato dell'Affaccata, nell'isola d'Elba. Annali delle Università toscane XX, 3–26.

558 Amaral, W.D.S., Santos, T.J.S., Wernick, E., 2011. Occurrence and geochemistry of metamafic rocks from the
559 Forquilha Eclogite Zone, Central Ceará (NE Brazil): geodynamic implications. Geological Journal 46, 137–155.

560 Angiboust, S., Langdon, R., Agard, P., Waters, D., Chopin, C., 2012. Eclogitization of the Monviso ophiolite (W. Alps)
561 and implications on subduction dynamics. Journal of Metamorphic Geology 30, 37–61.

562 Bambini, A.M., Brogi, A., Cornamusini, G., Costantini, A., Lazzarotto, A., 2009. Nuovi dati litostratigrafici e
563 biostratigrafici sulla Scaglia toscana nella Toscana meridionale (Area di Rapolano Terme). Bollettino della Società
564 Geologica Italiana 128, 669–693.

565 Barchi, M.R., 2010. The Neogene-Quaternary evolution of the Northern Apennines: crustal structure, style of
566 deformation and seismicity. In: Beltrando, M., Peccerillo, A., Mattei, M., Conticelli, S., Doglioni, C. (Eds.), The
567 Neogene-Quaternary Evolution of the Northern Apennines: Crustal Structure, Style of Deformation, Seismicity.
568 Journal of the Virtual Explorer 36(10), [//virtualexplorer.com.au/journal].

569 Bianco, C., Brogi, A., Caggianelli, A., Giorgetti, G., Liotta, D., Meccheri, M., 2015. HP-LT metamorphism in Elba
570 Island: Implications for the geodynamic evolution of the inner Northern Apennines (Italy). Journal of Geodynamics
571 91, 13–25.

572 Boccaletti, M., Elter, P., Guazzone, G.J.P., 1971. Plate tectonic models for the development of the western Alps and
573 Northern Apennines. Nature 234, 108–111.

574 Bortolotti, V., Fazzuoli, M., Pandeli, F., Principi, G., Babbini, A., Corti, S., 2001. Geology of Central and Eastern Elba
575 Island Italy. Ofioliti 26, 97–150 [+ 79–96].

576 Bortolotti, V., Pandeli, E., Principi, G., 2015. Carta geologica dell'Isola d'Elba, scala 1:25.000. Note
577 illustrative/Geological Map of Elba Island, 1:25.000 Scale. Explanatory notes, D.R.E.A.M., 74 pp.

578 Brogi, A., 2008. Kinematics and geometry of Miocene low-angle detachments and exhumation of the metamorphic
579 units in the hinterland of the Northern Apennines (Italy). Journal of Structural Geology 30, 2–20.

580 Brogi, A., Giorgetti, G., 2012. Tectono-metamorphic evolution of the siliciclastic units in the Middle Tuscan Range
581 (inner Northern Apennines): Mg-carpholite bearing quartz veins related to syn-metamorphic syn-orogenic foliation.
582 Tectonophysics 526–529, 167–184.
583 Brogi, A., Liotta, D., 2008. Highly extended terrains, lateral segmentation of the substratum, and basin development:
584 The middle-late Miocene Radicondoli Basin (inner northern Apennines, Italy). Tectonics 27, 1–20.
585 Brunet, C., Monié, P., Jolivet, L., Cadet, J.P., 2000. Migration of compression and extension in the Tyrrhenian Sea,
586 insights from $^{40}Ar/^{39}Ar$ ages on micas along a transect from Corsica to Tuscany. Tectonophysics 321, 127–155.
587 Caggianelli, A., Ranalli, G., Lavecchia, A., Liotta, D., Dini, A., 2014. Post-emplacement thermo-rheological history of
588 a granite intrusion and surrounding rocks: the Monte Capanne pluton, Elba Island, Italy. Geological Society,
589 London, Special Publications, 394, 129-144.
590 Canuti, P., Focardi, P., Sestini, G., 1965. Stratigrafia, correlazione e genesi degli Scisti Policromi dei Monti del Chianti
591 (Toscana). Bollettino della Società Geologica Italiana 84(6), 93–166.
592 Carmignani, L., Kligfield, R., 1990. Crustal extension in the Northern Apennines: the transition from compression to
593 extension in the Alpi Apuane core complex. Tectonics 9, 1275–1303.
594 Carmignani, L., Decandia, F.A., Disperati, L., Fantozzi, P.L., Lazzarotto, A., Liotta, D., Meccheri, M., 1994. Tertiary
595 extensional tectonics in Tuscany (Northern Apennines, Italy). Tectonophysics 238, 295–315.
596 Carmignani, L., Conti, P., Cornamusini, G., Meccheri, L., 2004. The internal Northern Apennines, the northern
597 Tyrrhenian Sea and the Sardinia-Corsica block. International Geological Congress 32, 59–77.
598 Carosi, R., Montomoli, C., 2002. Strutture tardo orogeniche e compressione parallela all'orogene in Appennino
599 Settentrionale: la struttura di interferenza polifasica di S. Giuliano (Unità di Santa Maria del Giudice, Monti Pisani).
600 Atti della Società Toscana di Scienze Naturali, Memorie Serie A, 2000-2001, 61–68.
601 Cerrina-Feroni, A., Martinelli, P., Perilli, N.M.L., 1991. Stratigrafia e struttura dell'Unità di Canetolo in Val Cedra
602 (Appennino parmense). Memorie Descrittive della Carta Geologica d'Italia 46, 301–312.
603 Deino, A., Keller, J.V.A., Minelli, G., Pialli, G., 1992. Datazioni $^{39}Ar/^{40}Ar$ del metamorfismo dell'Unità di Ortano-Rio
604 Marina (Isola d'Elba): risultati preliminari. Studi Geologici Camerti 1, 187–192.
605 Diener, J.F.A., Powell, R., 2012. Revised activity-composition models for clinopyroxene and amphibole. Journal of
606 Metamorphic Geology 30, 131–142.
607 Diener, J. F. A., Powell, R., White, R. W., & Holland, T. J. B., 2007. A new thermodynamic model for clino- and
608 orthoamphiboles in the system $Na_2O–CaO–FeO–MgO–Al_2O_3–SiO_2–H_2O–O$. Journal of Metamorphic
609 Geology 25(6), 631–656.

610 Duranti, S., Palmeri, R., Pertusati, P.C., Ricci, C.A., 1992. Geological evolution and metamorphic petrology of the
611 sequences of eastern Elba (Complex II). Acta Vulcanologica 2, 213–229.
612 Evans, B.W., 1990. Phase relations of epidote-blueschists. Lithos 25, 3–23.
613 Fazzuoli, M., Pandeli, E., Sandrelli, F., 1996. Nuovi dati litostratigrafici sulla Scaglia Toscana (scisti policromi) dei
614 Monti del Chianti (Appennino settentrionale). Atti della Società Toscana di Scienze Naturali, Memorie Serie A 103,
615 95–104.
616 Félix, C., Fransolet, A.M., 1972. Pseudomorphes à épidote s.l., paragonite, muscovite s.l., chlorite, albite,...de
617 porphyroblastes de lawsonite dans les glaucophanites de l'île de Groix (Bretagne - France). Annales de la Société
618 Géologique de Belgique 95, 323–334 [+ 345–391].
619 Fournier, M., Jolivet, L., Goffé, B., Dubois, R., 1991. Alpine Corsica metamorphic core complex. Tectonics 10, 1173–
620 1186.
621 Gagnevin, D., Daly, J.S., Horstwood, M.S.A., Whitehouse, M.J., 2011. In-situ zircon U-Pb, oxygen and hafnium
622 isotopic evidence for magma mixing and mantle metasomatism in the Tuscan Magmatic Province, Italy. Earth and
623 Planetary Science Letters 305, 45–56.
624 Geshi, N., Umino, S., Kumagai, H., Sinton, J.M., White, S.M., Kisimoto, K., Hilde, T.W., 2007. Discrete plumbing
625 systems and heterogeneous magma sources of a 24 km3 off-axis lava field on the western flank of East Pacific Rise,
626 14 S. Earth and Planetary Science Letters 258, 61–72.
627 Gillet, P., Goffé, B., 1988. On the significance of aragonite occurrences in the Western Alps. Contributions to
628 Mineralogy and Petrology 99, 70–81.
629 Giorgetti, G., Goffé, B., Memmi, I., Nieto, F., 1998. Metamorphic evolution of Verrucano metasediments in Northern
630 Apennines; new petrological constraints. European Journal of Mineralogy 10, 1295–1308.
631 Godard, G., 2009. Two orogenic cycles in eclogite-facies gneisses of the Southern Armorican Massif (France).
632 European Journal of Mineralogy 21, 1173–1190.
633 Green, E., Holland, T., Powell, R., 2007. An order-disorder model for omphacitic pyroxenes in the system jadeite-
634 diopside-hedenbergite-acmite, with applications to eclogitic rocks. American Mineralogist 92(7), 1181-1189.
635 Groppo, C., Castelli, D., 2010. Prograde P-T evolution of a lawsonite eclogite from the Monviso meta-ophiolite
636 (Western Alps): dehydration and redox reactions during subduction of oceanic FeTi-oxide gabbro. Journal of
637 Petrology 51, 2489–2514.
638 Hawthorne, F.C., Oberti, R., Harlow, G.E., Maresch, W.V., Martin, R.F., Schumacher, J.C., Welch, M.D., 2012.
639 Nomenclature of the amphibole supergroup. American Mineralogist 97, 2031–2048.

640 Hey, M.H., 1954. A new review of the chlorites. The Mineralogical Magazine and Journal of the Mineralogical
641 Society 30, 278–292.
642 Holdaway, M.J., 1972. Thermal stability of Al-Fe epidote as a function of fO2 and Fe content. Contributions to
643 Mineralogy and Petrology 37, 307–340.
644 Holland, T.J.B., Powell, R., 1998. An internally consistent thermodynamic data set for phases of petrological interest.
645 Journal of metamorphic Geology 16, 309–343.
646 Holland, T.J.B., Powell, R., 2003. Activity–composition relations for phases in petrological calculations: an asymmetric
647 multicomponent formulation. Contributions to Mineralogy and Petrology 145(4), 492-501.
648 Holland, T.J.B., Powell, R., 2011. An improved and extended internally consistent thermodynamic dataset for phases of
649 petrological interest, involving a new equation of state for solids. Journal of Metamorphic Geology 29, 333–383.
650 Holland, T.J.B., Baker, J.M., Powell, R., 1998. Mixing properties and activity-composition relationships of chlorites in
651 the system MgO-FeO-Al_2O_3-SiO_2-H_2O. European Journal of Mineralogy 10, 395–406.
652 Jacobs, J., Paoli, G., Rocchi, S., Ksienzyk, A.K., Sirevaag, H., Elburg, M.A., 2018. Alps to Apennines zircon roller
653 coaster along the Adria microplate margin. Scientific reports 8, 2704, doi: 10.1038/s41598-018-20979-w.
654 Kälin, O., Patacca, E., Renz, O., 1979. Jurassic pelagic deposits from Southeastern Tuscany; aspects of sedimentation
655 and biostratigraphic data. Eclogae Geologicae Helvetiae 72, 715–762.
656 Karsten, J.L., Delaney, J.R., Rhodes, J.M., Liias, R.A., 1990. Spatial and temporal evolution of magmatic systems
657 beneath the Endeavour Segment, Juan de Fuca Ridge: Tectonic and petrologic constraints. Journal of Geophysical
658 Research: Solid Earth 95 (B12), 19235–19256.
659 Keller, J.V.A., Pialli, G., 1990. Tectonics of the Island of Elba; a reappraisal. Bollettino della Società Geologica Italiana
660 109(2), 413-425.
661 Klein, E.M., 2004. Geochemistry of the Igneous Oceanic Crust, in: Holland, H.D. and Turekian, K.K. (Eds.), Treatise
662 on Geochemistry. Elsevier, Amsterdam, vol. 3, pp. 433–463.
663 Kligfield, R., Hunziker, J., Dallmayer, R.D., Schamel, S., 1986. Dating of deformation phases using K–Ar and
664 $^{40}Ar/^{39}Ar$ techniques: results from the Northern Apennines. Journal of Structural Geology 8, 781–798.
665 Kretz, R., 1983. Symbols for rock-forming minerals. American Mineralogist 68, 277–279.
666 Lee, J.Y., Marti, K., Severinghaus, J.P., Kawamura, K., Yoo, H.-S., Lee, J.B., Kim, J.S., 2006. A redetermination of the
667 isotopic abundances of atmospheric Ar. Geochimica et Cosmochimica Acta 70, 4507–4512.
668 Liotta, D., Brogi, A., Meccheri, M., Dini, A., Bianco, C., Ruggieri, G., 2015. Coexistence of low-angle normal and
669 high-angle strike- to oblique-slip faults during Late Miocene mineralization in eastern Elba Island (Italy).
670 Tectonophysics 660, doi: 10.1016/j.tecto.2015.06.025.

671 Liu, F., Yang, J, Dilek, Y., Xu, Z., Xu, X., Liang, F., Chen, S., 2015. Geochronology and geochemistry of basaltic lavas
672 in the Dongbo and Purang ophiolites of the Yarlung-Zangbo Suture zone: Plume-influenced continental margin-type
673 oceanic lithosphere in southern Tibet. Gondwana Research 27, 701–718.
674 López-Carmona, A., Abati, J., Pitra, P., Lee, J.K.W., 2014. Retrogressed lawsonite blueschists from the NW Iberian
675 Massif: P-T-t constraints from thermodynamic modelling and $^{40}Ar/^{39}Ar$ geochronology. Contributions to
676 Mineralogy and Petrology 167, 987, doi: 10.1007/s00410-014-0987-5.
677 Maineri, C., Benvenuti, M., Costagliola, P., Dini, A., Lattanzi, P., Ruggieri, G., Villa, I.M., 2003. Sericitic alteration at
678 the La Crocetta deposit (Elba Island, Italy): interplay between magmatism, tectonics and hydrothermal activity.
679 Mineralium Deposita 38, 67–86.
680 Molli, G., 2008. Northern Apennine-Corsica orogenic system: an updated overview, in: Siegesmund, S., Fügenschuh,
681 B., Froitzheim, N. (Eds.), Tectonic aspects of the Alpine-Dinaride-Carpathian system. Geological Society, London,
682 Special Publication 298, pp. 413–442.
683 Musumeci, G., Vaselli, L., 2012. Neogene deformation and granite emplacement in the metamorphic units of northern
684 Apennines (Italy): Insights from mylonitic marbles in the Porto Azzurro pluton contact aureole (Elba Island).
685 Geosphere 8, 470–490, http://doi.org/10.1130/GES00665.1.
686 Orozbaev, R., Hirajima, T., Bakirov, A., Takasu, A., Maki, K., Yoshida, K., Sakiev K., Bakirov A., Hirata T., Tagirid
687 M., Togonbaeva, A., 2015. Trace element characteristics of clinozoisite pseudomorphs after lawsonite in talc-
688 garnet-chloritoid schists from the Makbal UHP Complex, northern Kyrgyz Tian-Shan. Lithos 226, 98–115,
689 http://doi.org/10.1016/j.lithos.2014.10.008.
690 Pandeli, E., Puxeddu, M., Ruggieri, G., 2001. The metasiliciclastic-carbonate sequence of the Acquadolce Unit (eastern
691 Elba Island): new petrographic data and palaeogeographic interpretation. Ofioliti 26, 207–218.
692 Pearce, J.A., 2008. Geochemical fingerprinting of oceanic basalts with applications to ophiolite classification and the
693 search for Archean oceanic crust. Lithos 100, 14–48.
694 Pertusati, P., Raggi, G., Ricci, C.A., Duranti, S., Palmeri, R., 1993. Evoluzione post-collisionale dell'Elba centro-
695 orientale. Memorie della Società Geologica Italiana 49, 297–312.
696 Plesi G., Bianchi L., Chicchi S., Daniele G., 1993. Le Unità Liguri ed Emiliane della media Val di Taro e la loro
697 evoluzione strutturale. Atti Ticinensi di Scienze della Terra 36, 183–229.
698 Powell, R., Holland, T.J.B., 1988. An internally consistent dataset with uncertainties and correlations: 3. Applications to
699 geobarometry, worked examples and a computer program. Journal of metamorphic Geology 6, 173–204.

Renne, P.R., Mundil, R., Balco, G., Min, K., Ludwig, K.R., 2010. Joint determination of ^{40}K decay constants and $^{40}Ar^{*}/^{40}K$ for the Fish Canyon sanidine standard, and improved accuracy for $^{40}Ar/^{39}Ar$ geochronology. Geochimica et Cosmochimica Acta 74, 5349–5367.

Renne, P.R., Balco, G., Ludwig, K.R., Mundil, R., Min, K., 2011. Response to the comment by WH Schwarz et al. on "Joint determination of ^{40}K decay constants and $^{40}Ar^{*}/^{40}K$ for the Fish Canyon sanidine standard, and improved accuracy for $^{40}Ar/^{39}Ar$ geochronology" by PR Renne et al. (2010). Geochimica et Cosmochimica Acta 75, 5097–5100.

Rossetti, F., Faccenna, C., Jolivet, L., Goffé, B., Tecce, F., Brunet, C., Funiciello, R., Monié, P., 2001. Structural signature and exhumation P-T-t path of the Gorgona blueschist sequence (Tuscan Archipelago, Italy). Ofioliti 26, 175–186.

Rossetti, F., Faccenna, C., Jolivet, L., Goffé, B., Funiciello, R., 2002. Structural signature and exhumation P-T-t paths of the blueschist units exposed in the interior of the Northern Apennine chain, tectonic implications. Bollettino della Società Geologica Italiana 1, 829–842.

Rossetti, F., Glodny, J., Theye, T., Maggi, M., 2015. Pressure-temperature-deformation-time of the ductile Alpine shearing in Corsica: From orogenic construction to collapse. Lithos 218, 99-116.

Sun, S.S., McDonough, W.S., 1989. Chemical and isotopic systematics of oceanic basalts: implications for mantle composition and processes. Geological Society, London, Special Publications 42, 313–345.

Theye, T., Reinhardt, J., Goffé, B., Jolivet, L., Brunet, C., 1997. Fe- and Mg-carpholite from the Monte Argentario (Italy): first evidence for high-pressure metamorphism of the metasedimentary Verrucano sequence, and significance for P-T path reconstruction. European Journal of Mineralogy 9, 859–873.

Tsujimori, T., Sisson, V.B., Liou, J.G., Harlow, G.E., Sorensen, S.S., 2006. Very-low-temperature record of the subduction process: A review of worldwide lawsonite eclogites. Lithos 92, 609–624.

Ueda, H., Kawamura, M., Niida, K., 2000. Accretion and tectonic erosion processes revealed by the mode of occurrence and geochemistry of greenstones in the Cretaceous accretionary complexes of the Idonnappu Zone, southern central Hokkaido, Japan. Island Arc 9, 237–257.

Westerman, D.S., Dini, A., Innocenti, F., Rocchi, S., 2004. Rise and fall of a nested Christmas-tree laccolith complex, Elba Island, Italy, in: Breitkreuz, C., Petford, N. (Eds.), Physical Geology of High-Level Magmatic Systems. Geological Society, London, Special Publications 234, pp. 195–213.

White, R.W., Powell, R., Holland, T.J.B., 2007. Progress relating to calculation of partial melting equilibria for metapelites. Journal of Metamorphic Geology 25, 511–527.

Figure

Click here to download high resolution image

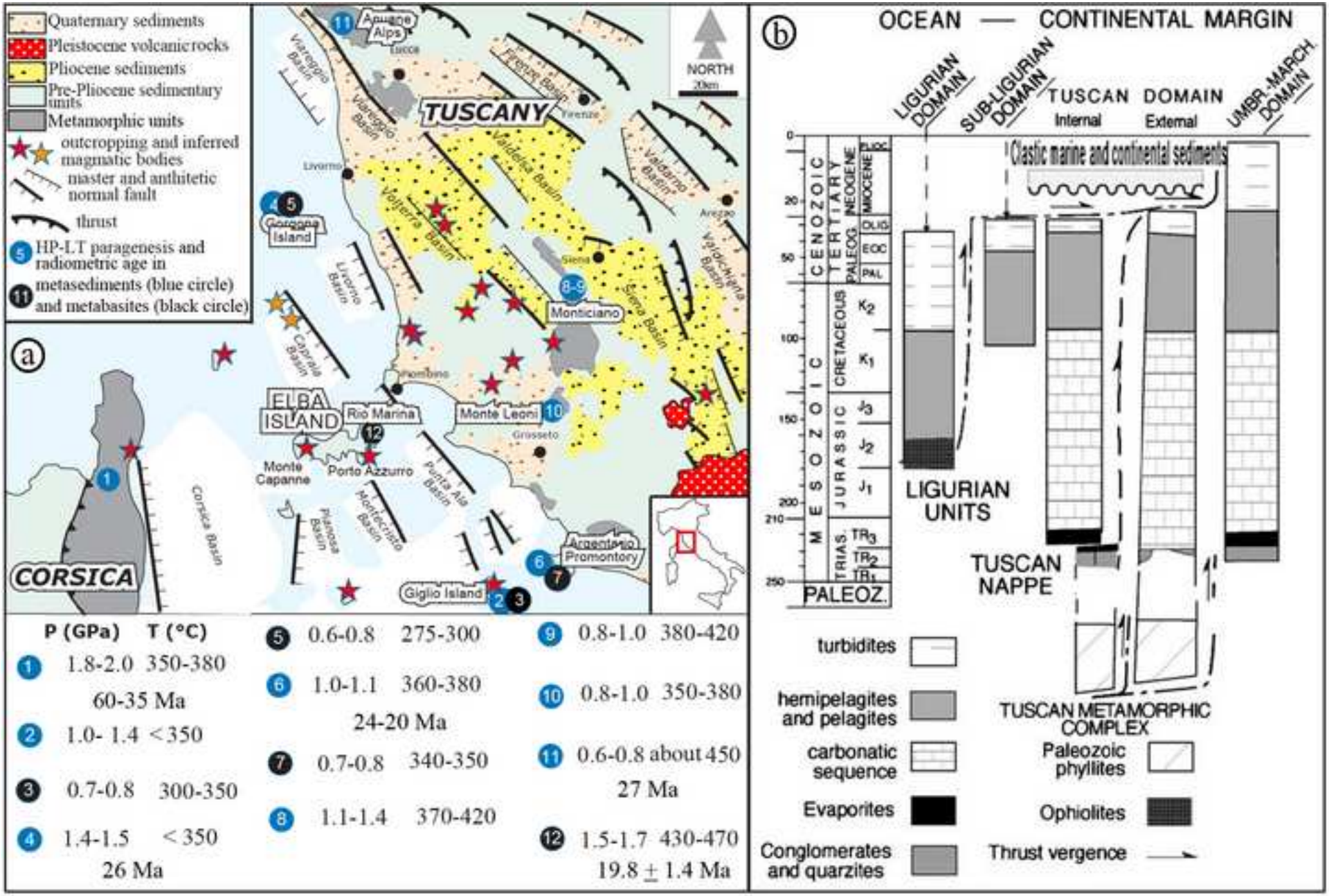

FIGURE 1

Figure

Click here to download high resolution image

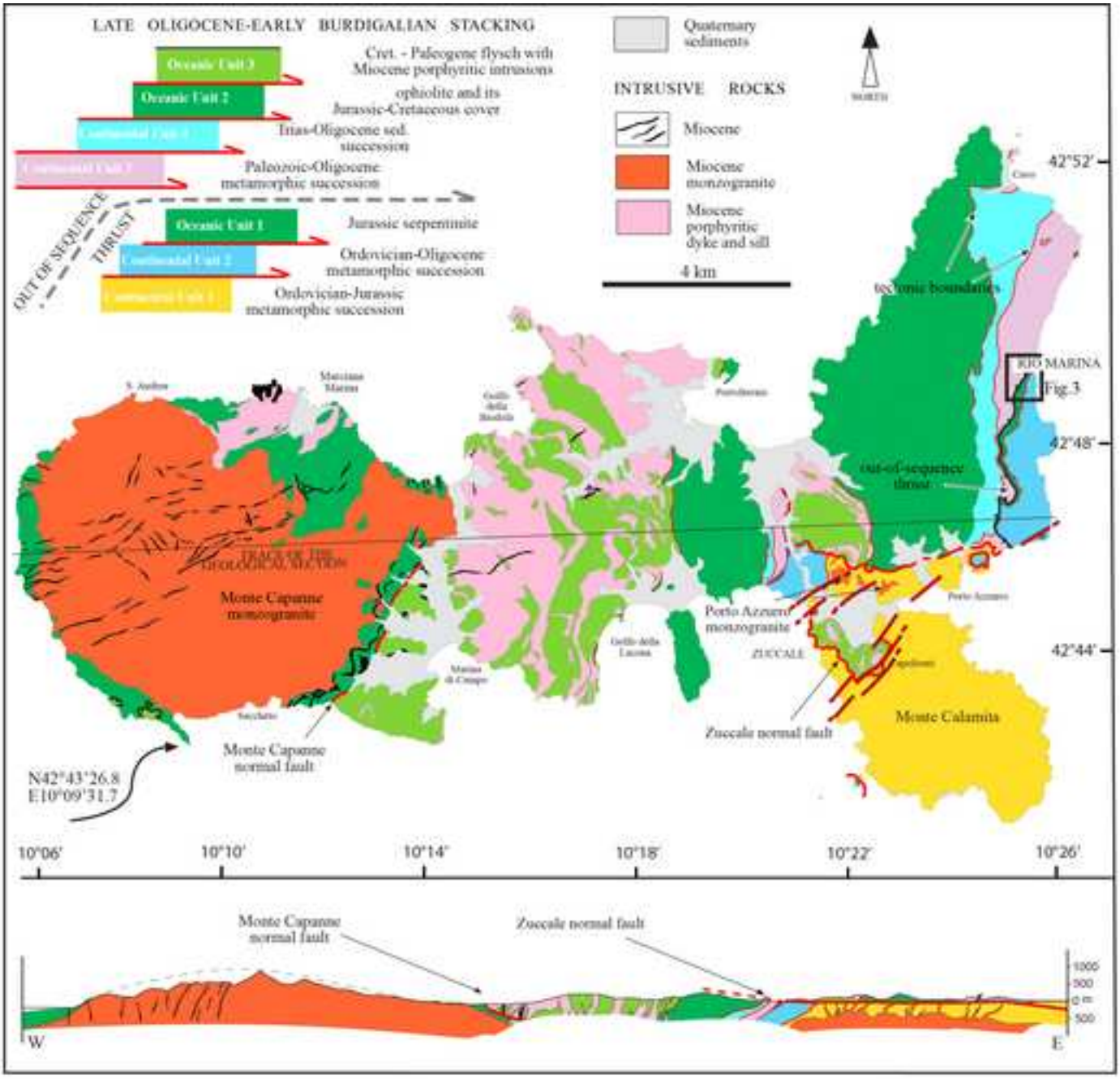

FIGURE 2

Figure

Click here to download high resolution image

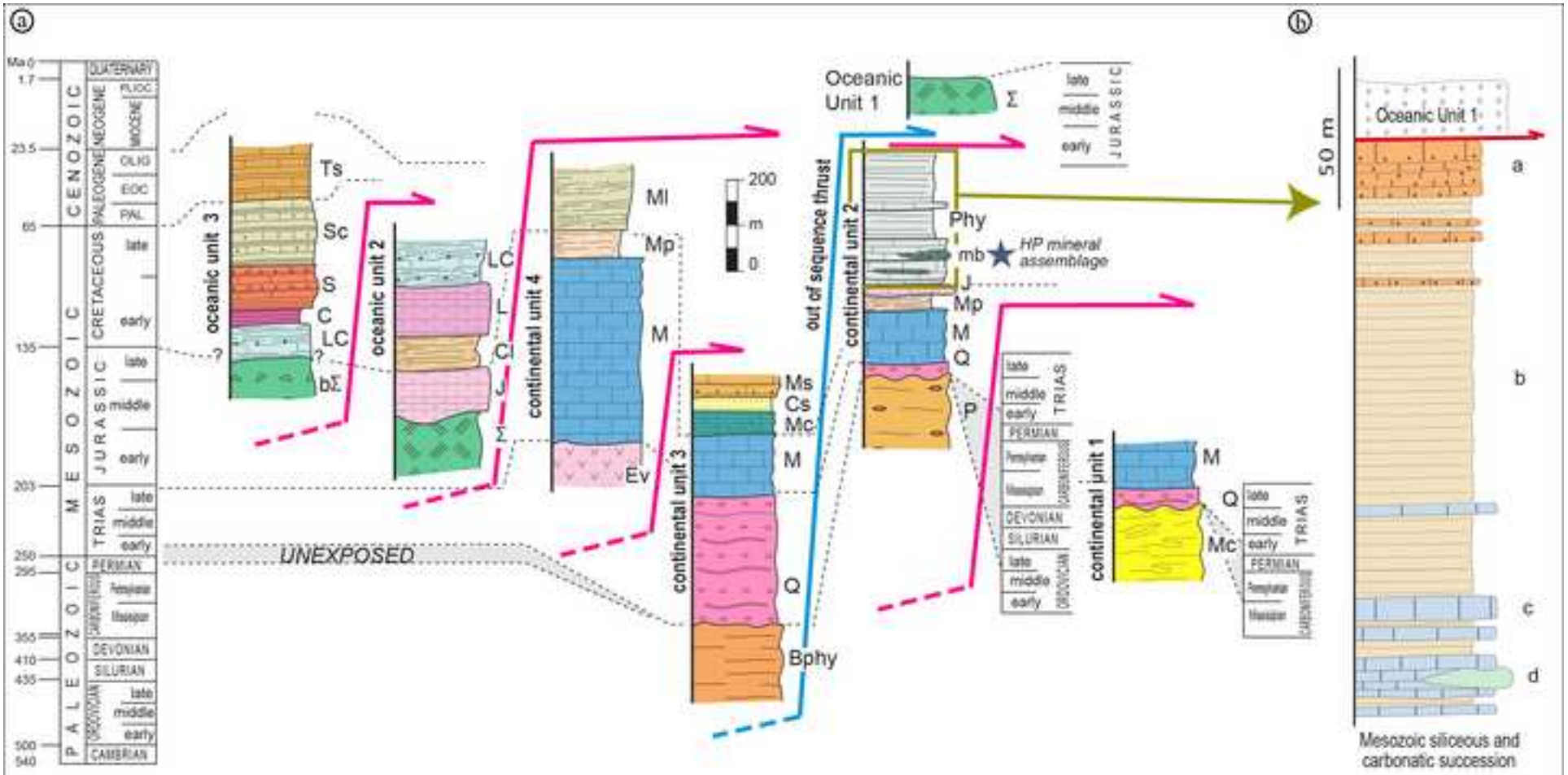

Oceanic Unit 3: bΣ = Breccia of ophiolitic rocks; LC = limestone and shale (Palombini Shales Fm); C = shale (Varicoloured Shales Fm); S = sandstone and shale (Ghiaieto Sandstones Fm); Sc = sandstone and marlstone (Marina di Campo Fm); Ts = shale with limestone and marlstone (Colle Reciso Fm). Oceanic Unit 2: Σ = serpentinite; J = radiolarite (Mt. Alpe Cherts Fm); Cl = calcilutite and cherty limestone (Nisportino Fm); L = cherty limestone (Calpionella Limestones Fm); LC = limestone and shale (Palombini Shales Fm). Continental Unit 4: Ev = evaporite (Calcare Cavernoso Fm); M = massive and cherty limestone and dolostone (Pania di Corfino Fm, Mt. Cetona Fm, Calcare Massiccio Fm, Grotta Giusti Limestones, Rosso Ammonitico Fm, Limano cherty Limestones Fm); Mp = marls (Posidonia Marlstones Fm); Ml = Varicoloured Shales (Cavo Fm). Continental Unit 3: Bphy = black phyllite (Rio Marina Fm); Q = quartzite and phyllite (Verruca Fm, Mt. Serra quartzite Fm); M = marble (Valle Giove Limestones Fm; Capo Pero Limestone Fm; Capo Castello Calcschists Fm); Mc = cherty marble; Cs = calcschist and phyllite (Varicoloured Sericitic Schist Fm); Ms = metasandstone and phyllite (Pseudomacigno Fm). Continental Unit 2: P = porphyroids, quartzite and phyllite (Ortano Unit); Q = quartzite; M = massive and cherty limestone and dolostone (Valdana marble Fm); Mp = marls (Posidonia Marlstones Fm); J = radiolarite; Phy = calcschist with interbedded metabasite (Mb) and phyllite (Acquadolce Unit). Oceanic Unit 1: Σ = serpentinite. Continental Unit 1: Mc = micaschist (Mt. Calamita Fm); Q = quartzite and phyllite (Quarziti di Barabarca Fm); M = dolostone (Crystalline dolostone and dolomitic limestone Fm). Formational names after Bortolotti et al. (2001) and Garfagnoli et al. (2005). The star indicates the structural levels of the analyzed metabasite.

Figure 3

Figure

Click here to download high resolution image

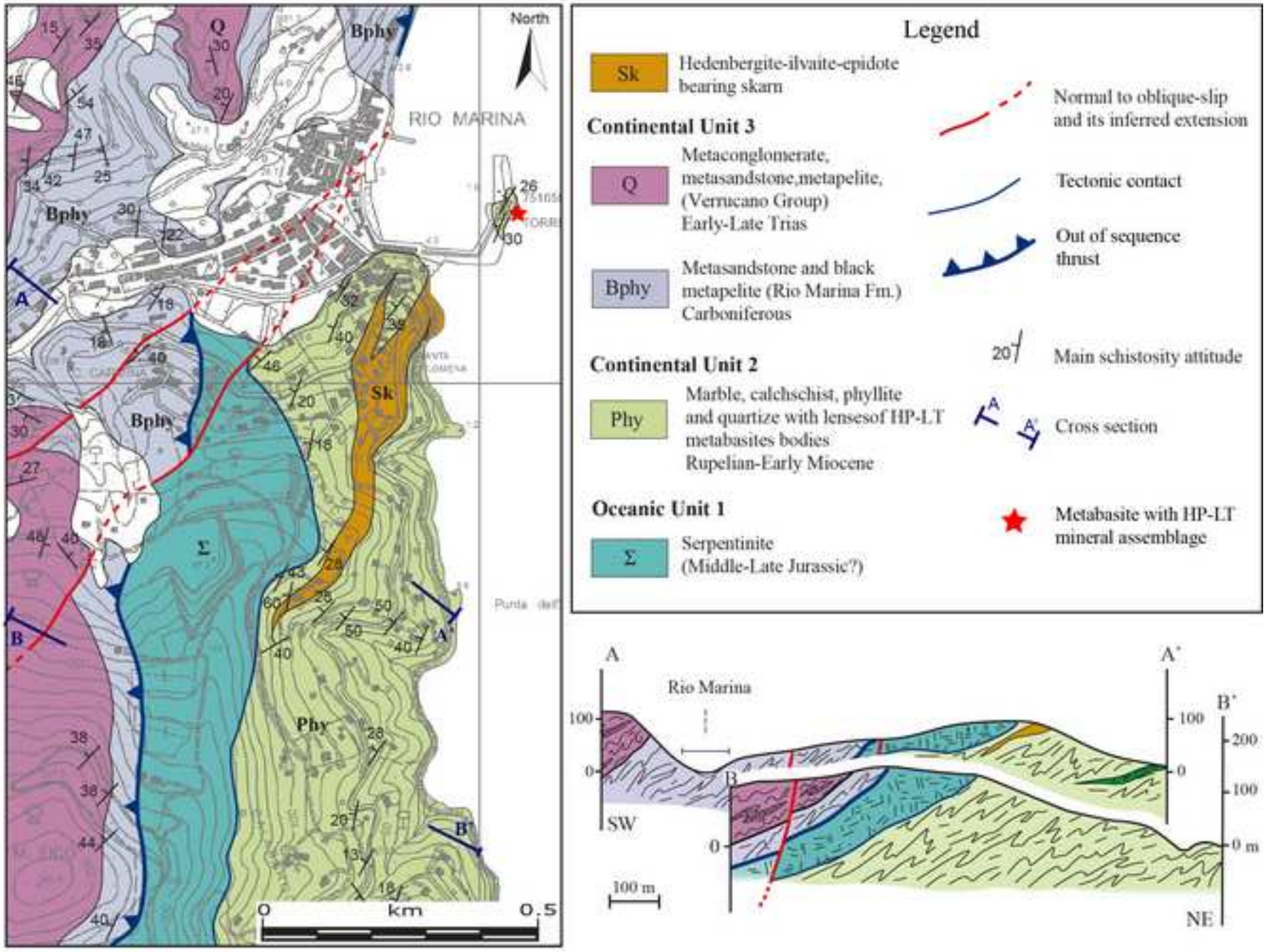

Figure 4

Figure
Click here to download high resolution image

Figure 5

Figure
Click here to download high resolution image

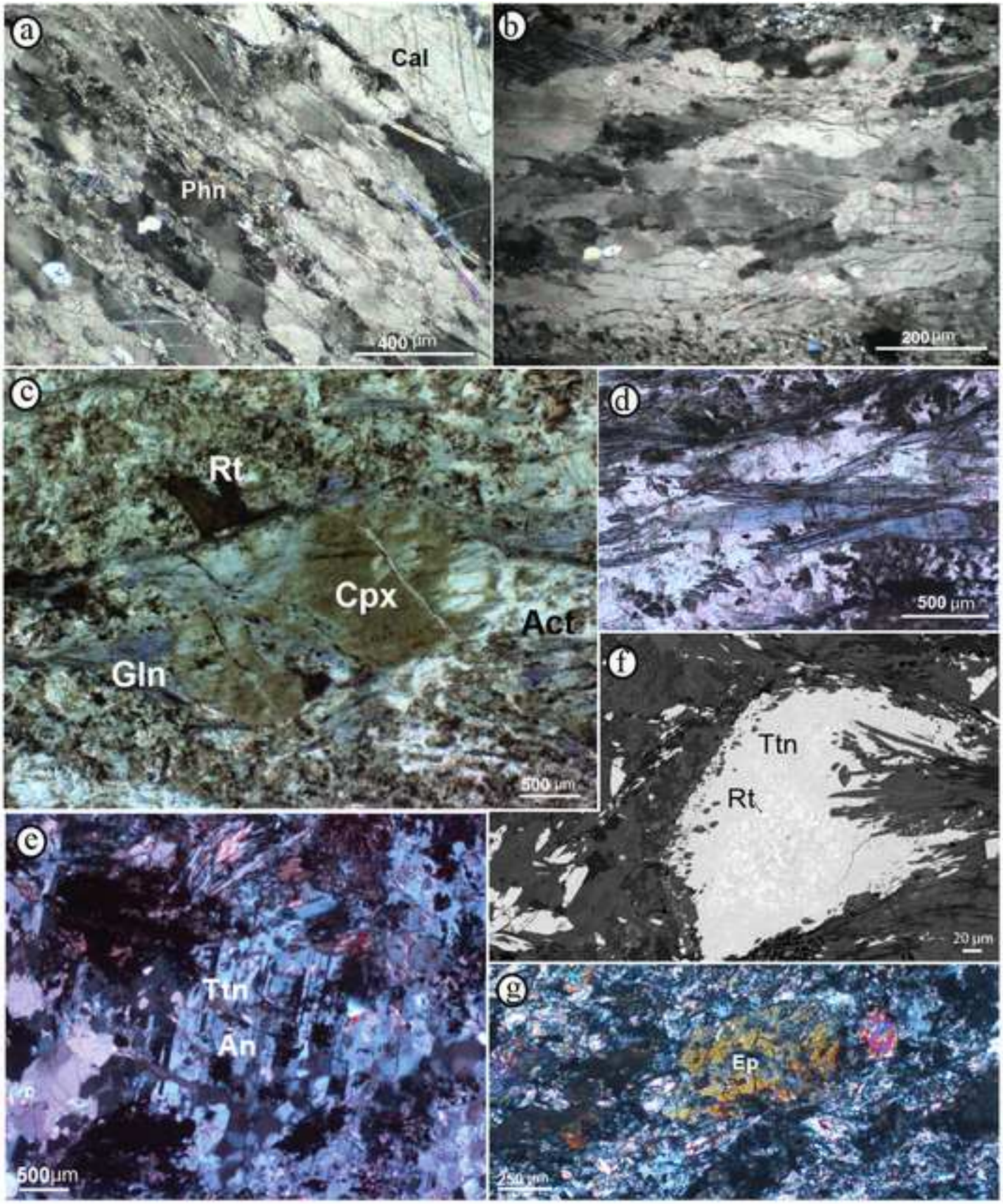

Figure 6

Figure

Click here to download high resolution image

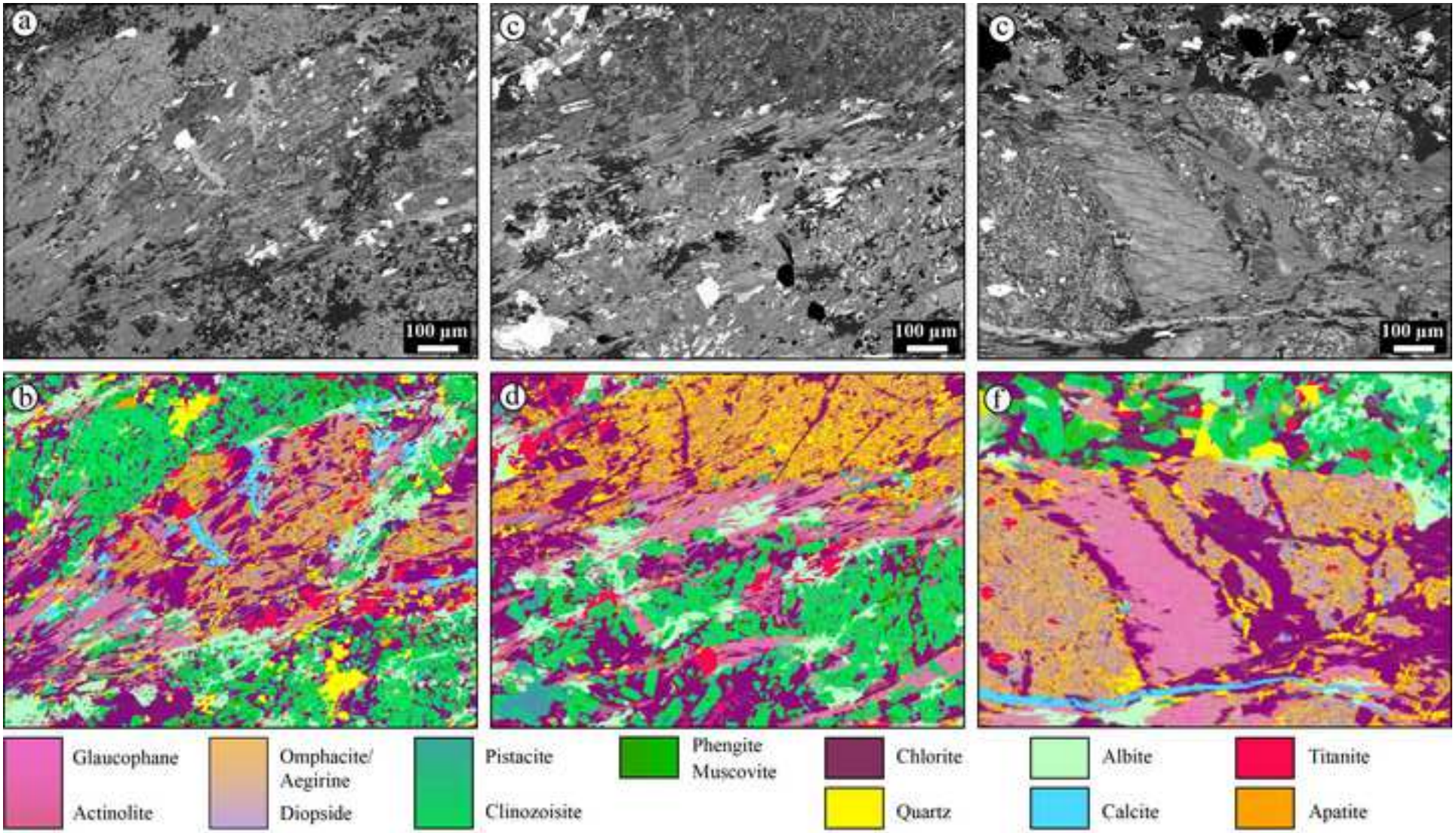

Figure 7

Figure
Click here to download high resolution image

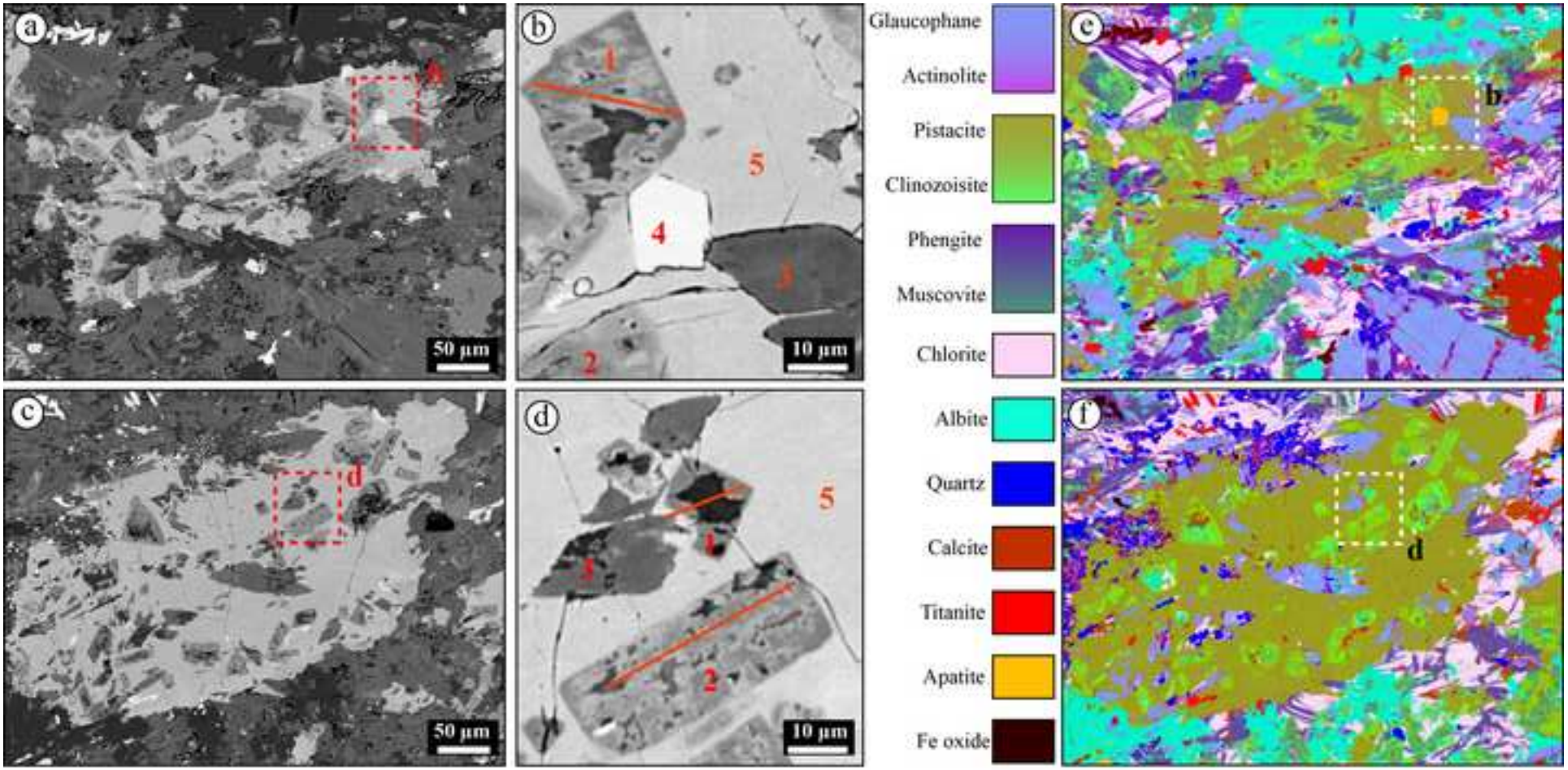

Figure 8

Figure
Click here to download high resolution image

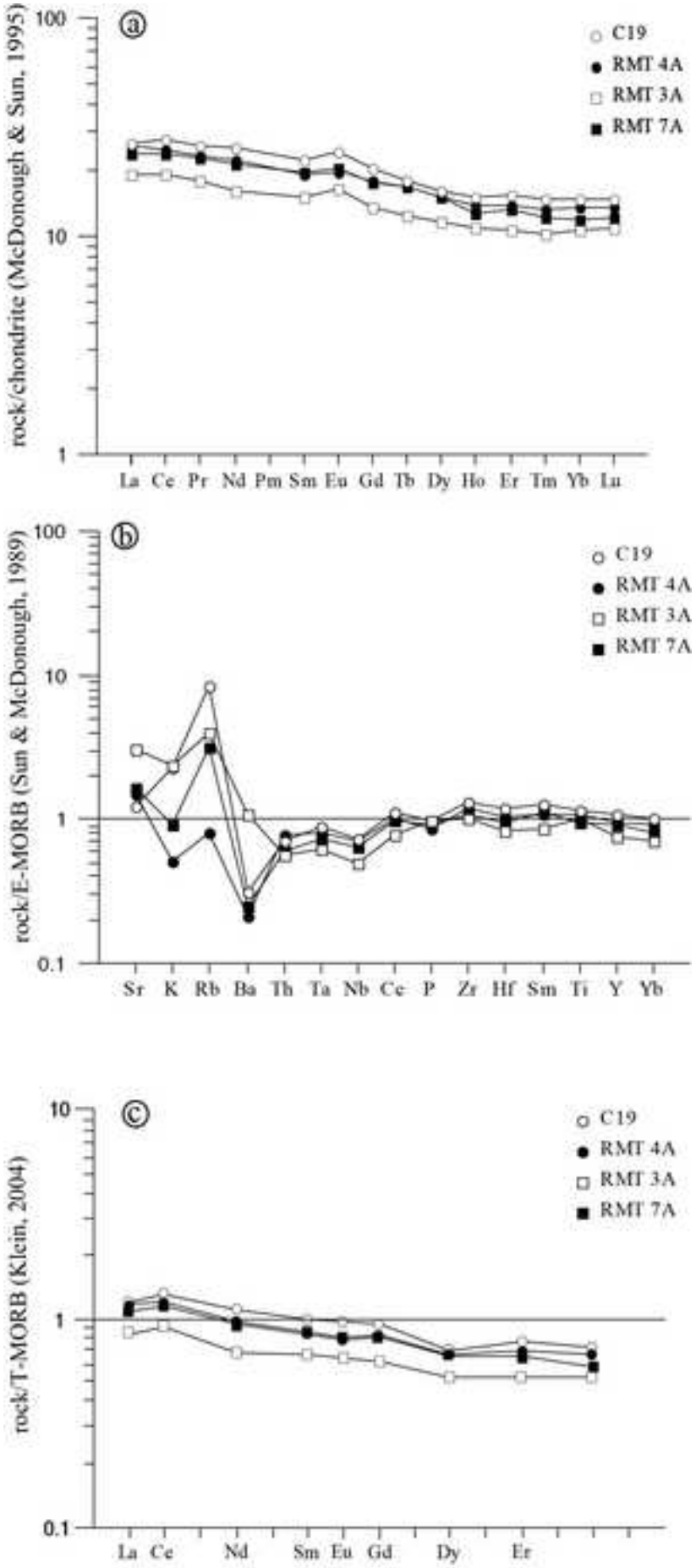

Figure 9

Figure
Click here to download high resolution image

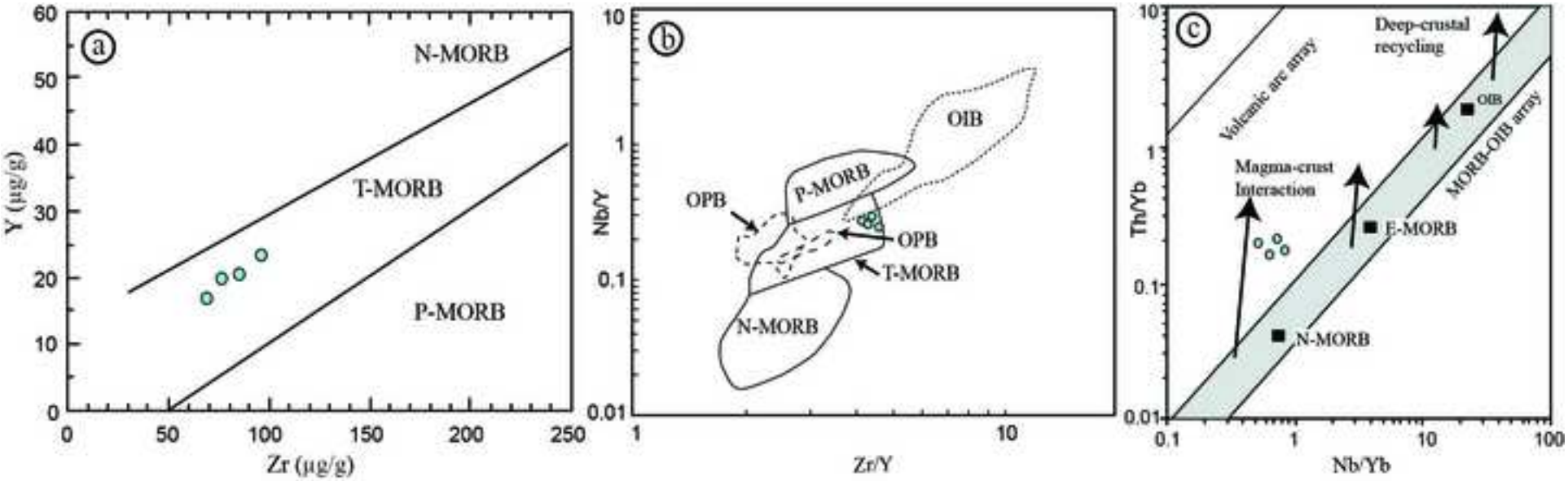

Figure 10

Figure
Click here to download high resolution image

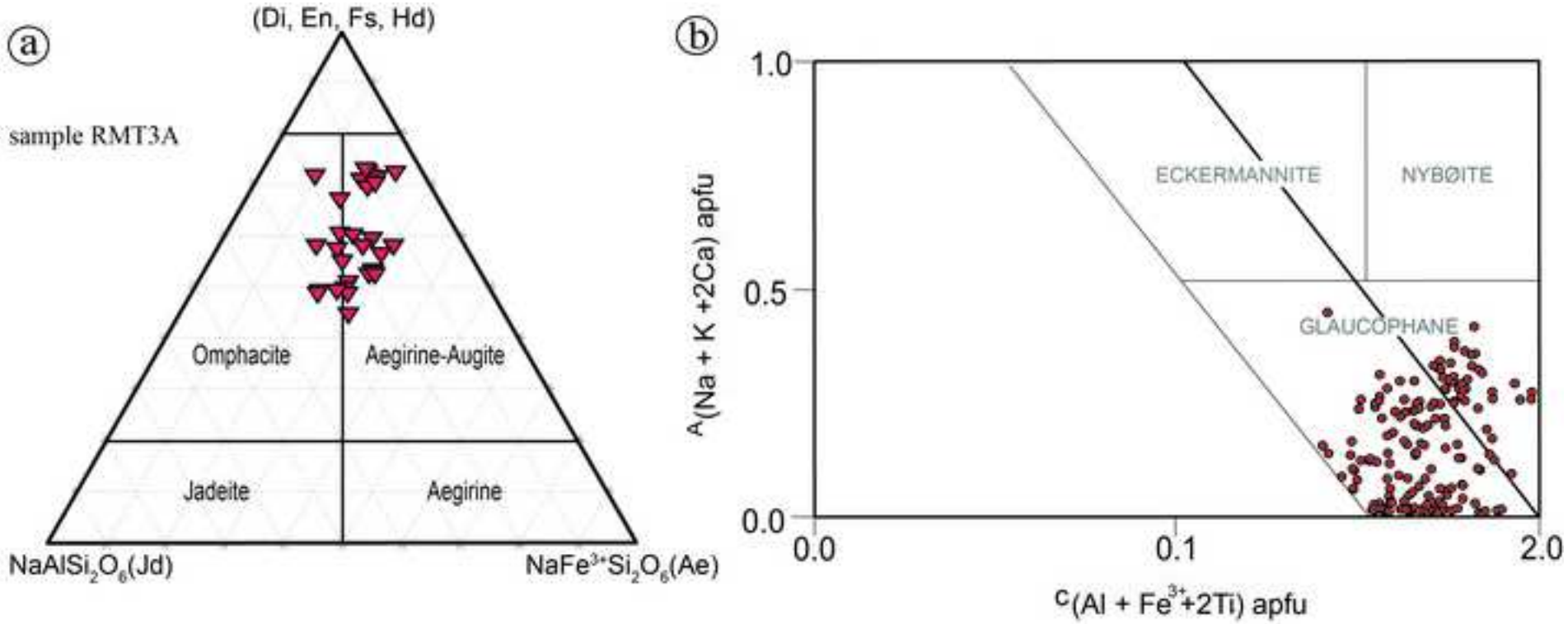

Figure 11

Figure
Click here to download high resolution image

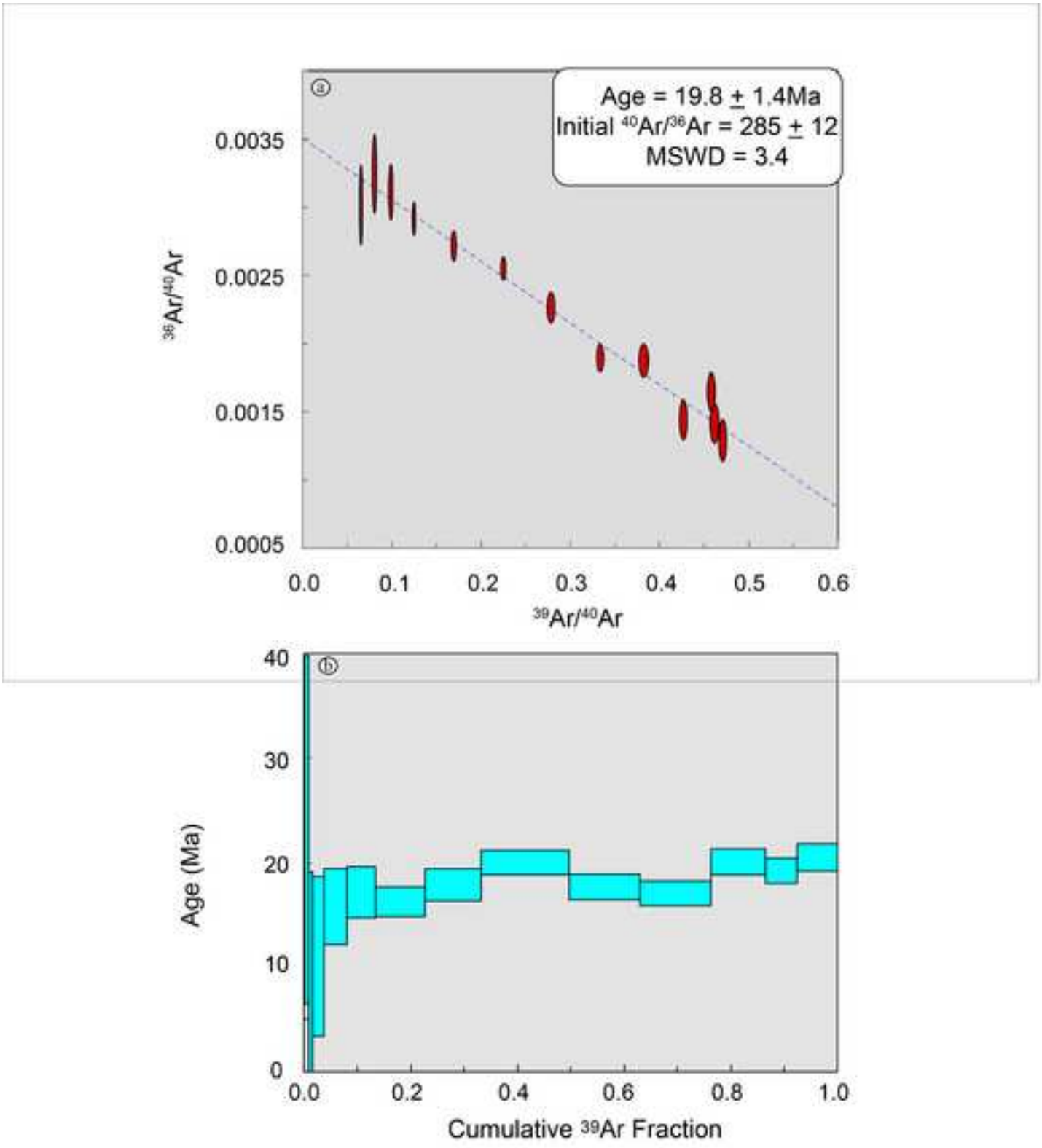

Figure 12

Figure
Click here to download high resolution image

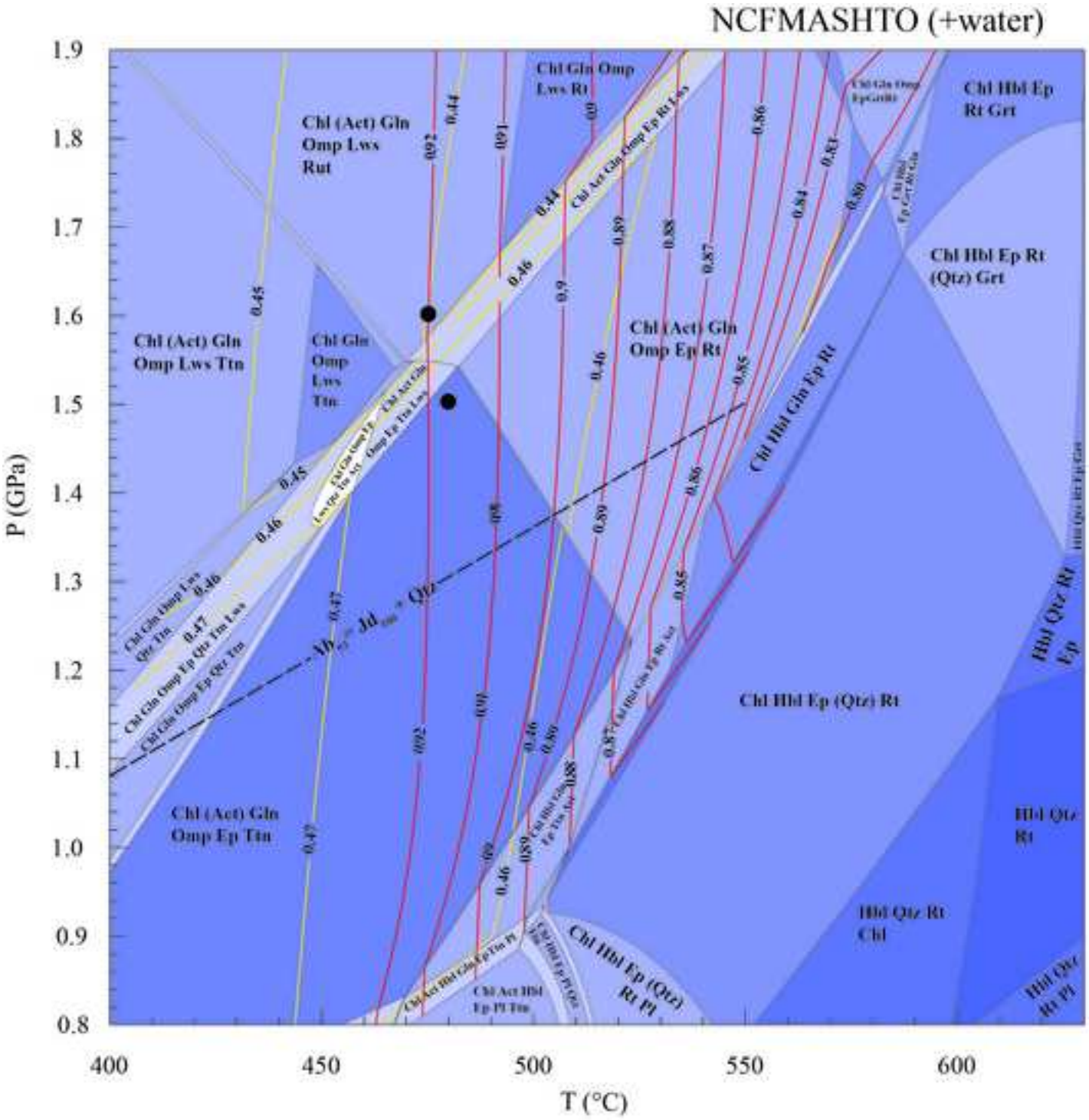

Figure 13

Figure
Click here to download high resolution image

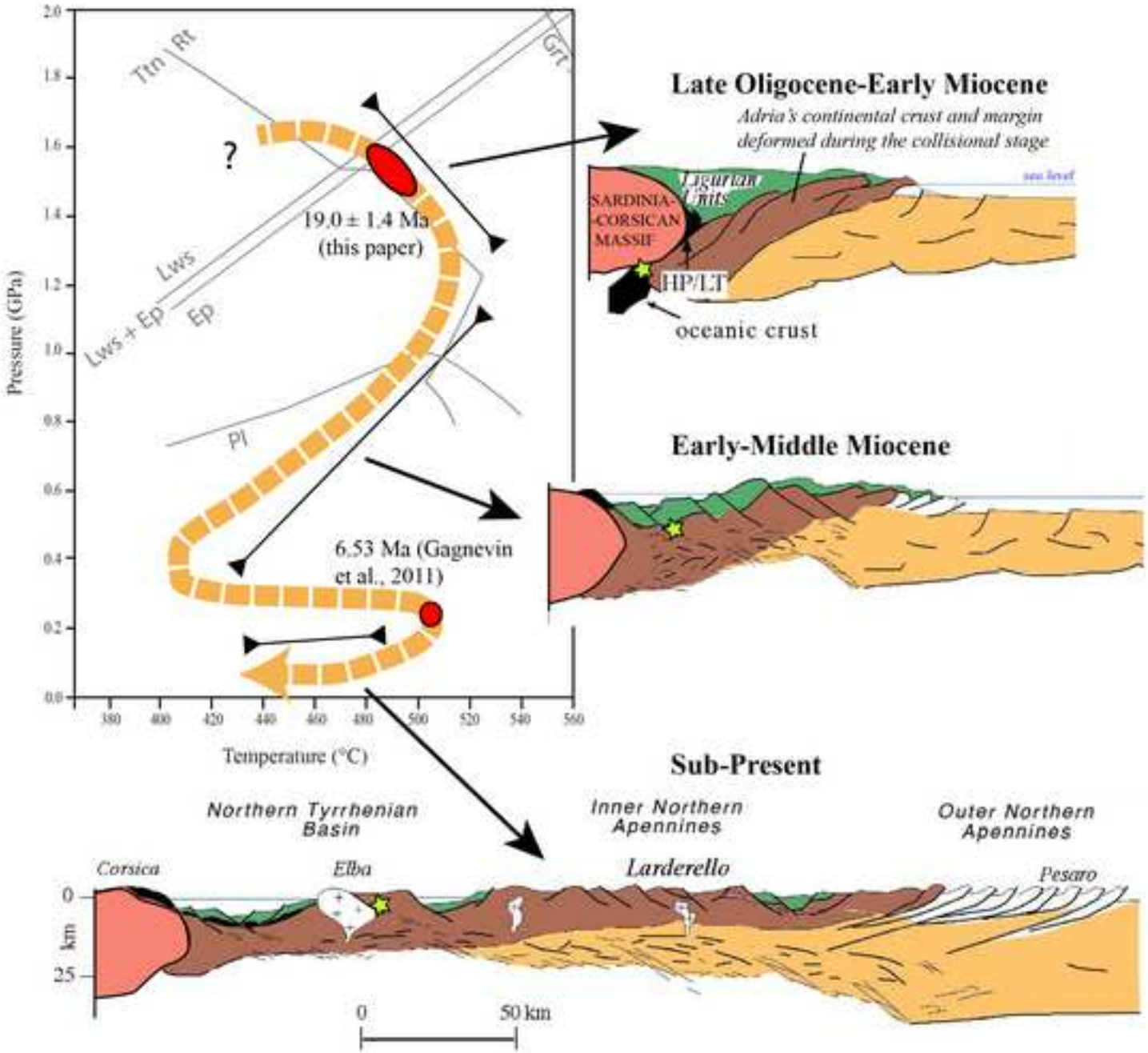

Figure 14

Table

Click here to download Table: Tab.1.pdf

Tab.1 Bulk-rock composition of metabasite sample RMT3A (wt%)

SiO_2	TiO_2	Al_2O_3	Cr_2O_3	Fe_2O_3t	MnO	MgO	CaO	Na_2O	K_2O	P_2O_5	L.O.I.	Total	X_{Mg}
42.54	0.97	16.89	0.01	8.67	0.12	10.86	9.25	2.75	0.55	0.12	7.27	100	0.71

Table

Click here to download Table: Tab.2.pdf

Tab. 2- Trace-element composition of metabasite samples from Rio Marina area

µg/g	C19	RMT4A	RMT3A	RMT7A
V	163	159	142	160
Cr	240	250	210	240
Co	41	41	27	38
Ni	130	130	110	120
Cu	60	80	80	70
Zn	50	40	110	60
Ga	16	14	13	14
Ge	1.4	1.3	1.5	1.4
As	< 5	< 5	< 5	< 5
Rb	42	4	20	16
Sr	193	232	475	253
Y	23.7	20.9	16.8	20.1
Zr	96	87	74	80
Nb	6	5.8	4.1	5.3
Mo	< 2	< 2	< 2	< 2
Ag	< 0.5	< 0.5	< 0.5	< 0.5
In	< 0.1	< 0.1	< 0.1	< 0.1
Sn	< 1	< 1	< 1	< 1
Sb	2.8	3	2.8	2.8
Cs	2.4	0.9	3	1.9
Ba	18	12	62	14
La	6.36	6.21	4.51	5.69
Ce	16.9	15.4	11.8	14.7
Pr	2.43	2.16	1.67	2.13
Nd	11.6	10.3	7.3	9.7
Sm	3.29	2.83	2.22	2.89
Eu	1.36	1.11	0.92	1.14
Gd	4.08	3.57	2.68	3.51
Tb	0.65	0.61	0.45	0.61
Dy	3.97	3.73	2.88	3.72
Ho	0.83	0.77	0.6	0.7
Er	2.47	2.23	1.7	2.1
Tm	0.367	0.332	0.256	0.304
Yb	2.36	2.19	1.7	1.9
Lu	0.366	0.338	0.27	0.303
Hf	2.4	2.1	1.7	1.9
Ta	0.42	0.38	0.29	0.34
W	< 0.5	< 0.5	< 0.5	< 0.5
Tl	0.2	< 0.05	0.14	0.09
Pb	< 5	< 5	27	13
Bi	< 0.1	< 0.1	< 0.1	< 0.1
Th	0.43	0.46	0.34	0.36
U	0.16	0.32	0.28	0.17
(Ce/Yb)N	1.87	1.84	1.81	2.02
(La/Yb)N	1.82	1.92	1.79	2.02
Eu/Eu*	1.13	1.07	1.15	1.09
Y/Nb	3.95	3.6	4.1	3.79
Zr/Nb	16	15	18.05	15.09
Ti/Y	290.85	309.74	367.49	289.26
Zr/Y	4.05	4.16	4.4	3.98
La/Sm	1.93	2.19	2.03	1.97

Table
Click here to download Table: Tab.3.pdf

Tab. 3 Representative microprobe analyses for metabasite sample RMT3A

	Cpx		Gln 1**		Gln 2 cores***		Gln 2 rims***		Ep		Czo****		Ms****		Phn		Chl		Ab		Mag
	av	±σ	av(11)	±σ	av(21)	±σ	av(24)	±σ	av(40)	±σ	av(12)	±σ	av	±σ	av	±σ	av	±σ	av	±σ	
SiO_2	54.62	0.54	57.78	0.66	58.26	0.24	57.94	0.37	37.26	0.71	38.60	0.66	44.63	0.15	50.04	1.25	30.22	0.30	68.39	0.72	0.21
TiO_2	0.08	0.07	0.15	0.08	0.11	0.08	0.15	0.10	0.08	0.07	0.14	0.10	0.14	0.05	0.04	0.01	0.03	0.03	0.02	0.02	0.09
Al_2O_3	5.54	1.14	10.01	0.55	9.70	0.63	9.23	0.72	22.39	0.78	30.36	1.66	36.87	0.44	26.34	1.11	19.16	1.44	19.96	0.55	0.36
Cr_2O_3	0.28	0.27	0.02	0.02	0.01	0.01	0.01	0.01	0.02	0.02	0.03	0.03	0.01	0.01	0.02	0.02	0.11	0.07	0.01	0.01	0.04
FeOt	10.62	0.73	10.47	0.35	10.42	0.52	10.98	0.56	13.68	0.69	4.83	2.24	2.06	0.26	4.74	0.30	16.64	1.93	0.22	0.26	88.86
MnO	0.20	0.05	0.18	0.06	0.18	0.04	0.18	0.05	0.23	0.16	0.11	0.05	0.01	0.01	0.02	0.02	0.28	0.05	0.01	0.01	0.00
MgO	8.60	0.51	10.97	0.34	11.29	0.37	11.36	0.40	0.00	0.00	0.00	0.00	0.13	0.13	3.46	0.25	20.72	2.19	0.12	0.27	0.02
CaO	12.72	1.07	0.91	0.33	0.78	0.27	1.11	0.58	22.61	0.52	23.62	0.64	0.31	0.17	0.04	0.03	0.21	0.42	0.38	0.41	0.21
Na_2O	6.55	0.55	6.80	0.27	6.47	0.28	6.23	0.45	0.01	0.02	0.06	0.04	0.54	0.29	0.08	0.01	0.11	0.35	11.63	0.50	0.00
K_2O	0.21	0.16	0.03	0.03	0.04	0.03	0.06	0.07	0.01	0.02	0.08	0.14	9.50	0.25	10.39	0.13	0.05	0.13	0.05	0.05	0.00
F			0.06	0.08	0.13	0.14	0.09	0.11	0.07	0.13	0.01	0.02	0.03	0.05	0.11	0.04	0.10	0.09			
Total*	100.33	0.55	97.34	0.72	97.33	0.49	97.30	0.54	96.34	1.14	97.82	0.49	98.78	0.42	99.72	0.08	89.13	1.01	100.87	0.77	96.43
Si	1.988	0.020	7.926	0.088	7.980	0.020	7.961	0.038	2.988	0.022	2.966	0.024	6.004	0.015	6.768	0.147	5.802	0.466	2.969	0.020	0.009
Al	0.237	0.048	1.619	0.096	1.565	0.100	1.494	0.112	2.117	0.055	2.749	0.124	5.846	0.069	4.200	0.190	4.345	0.358	1.021	0.024	0.017
Ti	0.002	0.002	0.015	0.008	0.011	0.008	0.016	0.010	0.005	0.004	0.008	0.006	0.014	0.005	0.004	0.001	0.004	0.004	0.000	0.001	0.003
Cr	0.008	0.008	0.002	0.002	0.001	0.001	0.001	0.001	0.002	0.001	0.002	0.002	0.001	0.001	0.002	0.002	0.017	0.011	0.000	0.000	0.001
Fe^{3+}	0.246	0.055	0.362	0.087	0.341	0.074	0.389	0.095	0.917	0.047	0.310	0.147					2.204	0.261	0.008	0.010	1.977
Fe^{2+}	0.078	0.051	0.839	0.073	0.835	0.044	0.856	0.062					0.232	0.030	0.536	0.036	0.474	0.194			0.974
Mn	0.006	0.001	0.021	0.007	0.020	0.004	0.021	0.006	0.015	0.011	0.007	0.003	0.001	0.001	0.003	0.002	0.045	0.008	0.000	0.000	0.000
Mg	0.467	0.029	2.243	0.060	2.305	0.078	2.326	0.085	0.000	0.000	0.000	0.000	0.026	0.026	0.698	0.049	5.944	0.654	0.008	0.018	0.001
Ca	0.496	0.043	0.133	0.049	0.114	0.040	0.163	0.085	1.943	0.067	1.945	0.043	0.045	0.024	0.006	0.004	0.042	0.080	0.018	0.019	0.009
Na	0.462	0.036	1.808	0.064	1.719	0.072	1.661	0.118	0.002	0.003	0.008	0.006	0.140	0.075	0.020	0.003	0.040	0.124	0.979	0.038	0.000
K	0.010	0.007	0.005	0.006	0.005	0.005	0.010	0.012	0.001	0.002	0.008	0.014	1.631	0.050	1.792	0.029	0.011	0.034	0.003	0.003	0.001
∑cat	4.000	0.000	14.973	0.029	14.914	0.016	14.916	0.036	7.991	0.028	8.004	0.016	13.944	0.050	14.033	0.068	18.933	0.269	5.007	0.012	2.991
F			0.026	0.028	0.056	0.059	0.039	0.044	0.018	0.032	0.001	0.004	0.012	0.020	0.047	0.017	0.057	0.054			
X_{Mg}	0.854	0.076	0.725	0.019	0.729	0.016	0.726	0.019					0.092	0.076	0.564	0.035	0.919	0.031			

Supplementary material

Click here to download Table: SM1.pdf

SM1: Representative microprobe analyses for metabasite sample C19

	Cpx		Gln cores***		Gln rims***		Czo****		Ms****		Chl		Ab		An		Ttn	
	av(18)	±σ	av(34)	±σ	av(41)	±σ	av(6)	±σ	av(8)	±σ	av(56)	±σ	av(8)	±σ	av(8)	±σ	av(9)	±σ
SiO_2	54.79	1.29	56.22	0.72	57.15	0.69	38.48	0.29	45.72	0.70	30.04	2.75	67.80	1.26	43.38	0.35	32.68	4.15
TiO_2	0.04	0.05	0.24	0.13	0.22	0.14	0.38	0.21	0.20	0.09	0.03	0.03	0.21	0.36	0.23	0.22	37.23	3.52
Al_2O_3	4.10	1.49	8.71	1.35	7.93	0.92	29.15	1.13	38.11	0.83	19.23	1.34	19.80	0.69	36.22	0.66	1.27	0.61
Cr_2O_3							0.01	0.01	0.01	0.02	0.11	0.07	0.00	0.00	0.02	0.02	0.01	0.01
FeOt	9.90	0.51	12.30	1.91	13.92	1.79	5.03	1.41	0.72	0.16	16.65	1.95	0.19	0.03	0.51	0.73	0.82	0.64
MnO	0.29	0.05	0.11	0.04	0.09	0.04	0.10	0.02	0.02	0.03	0.28	0.05	0.01	0.01	0.01	0.03	0.03	0.03
MgO	9.55	1.04	10.37	0.50	10.27	0.55	0.00	0.00	0.19	0.05	20.81	2.12	0.01	0.01	0.22	0.86	0.43	0.76
CaO	14.70	2.38	3.61	0.98	0.82	0.40	23.66	0.13	0.81	0.76	0.21	0.42	0.48	0.34	19.17	2.10	26.84	2.22
Na_2O	5.55	1.03	6.30	0.27	6.37	0.35	0.05	0.01	0.30	0.19	0.07	0.17	11.66	1.22	0.41	0.24	0.28	0.47
K_2O	0.08	0.08	0.03	0.01	0.02	0.03	0.05	0.00	9.48	1.42	0.05	0.14	0.03	0.03	0.06	0.05	0.02	0.02
F			0.04	0.05	0.06	0.07	0.13	0.09	0.05	0.10	0.10	0.09					0.19	0.17
Total*	98.99	0.72	97.93	5.93	96.84	4.95	98.88	3.32	100.12	4.37	88.25	9.15	100.20	3.94	100.23	5.26	99.78	12.60
Si	2.010	0.044	7.790	8.002	8.016	8.002	2.977	0.005	6.015	0.016	5.774	0.422	2.963	0.015	2.004	0.026	4.210	0.433
Al	0.177	0.064	1.520	1.429	1.312	1.188	2.657	0.087	5.908	0.029	4.365	0.328	1.020	0.024	1.971	0.025	0.193	0.093
Ti	0.001	0.001	0.017	0.026	0.024	0.022	0.022	0.012	0.019	0.009	0.004	0.004	0.007	0.012	0.008	0.008	3.620	0.387
Cr							0.001	0.001	0.001	0.002	0.017	0.011	0.000	0.000	0.001	0.001	0.001	0.001
Fe^{3+}	0.199	0.090	0.269	0.203	0.338	0.481	0.326	0.094			2.208	0.262	0.007	0.001	0.020	0.029	0.070	0.055
Fe^{2+}	0.105	0.084	1.450	1.247	1.294	1.234	0.000	0.000	0.079	0.017	0.474	0.195					0.018	0.014
Mn	0.009	0.002	0.010	0.013	0.011	0.014	0.007	0.001	0.002	0.004	0.046	0.008	0.000	0.000	0.000	0.001	0.004	0.004
Mg	0.522	0.059	2.333	2.210	2.148	2.185	0.000	0.000	0.036	0.009	5.973	0.625	0.001	0.001	0.015	0.060	0.082	0.145
Ca	0.578	0.096	0.113	0.174	0.123	0.155	1.962	0.022	0.114	0.104	0.042	0.081	0.023	0.016	0.949	0.099	3.717	0.364
Na	0.395	0.071	1.586	1.695	1.733	1.719	0.008	0.001	0.075	0.047	0.025	0.061	0.987	0.084	0.037	0.022	0.070	0.117
K	0.004	0.004	0.004	0.005	0.003	0.003	0.005	0.000	1.593	0.258	0.011	0.034	0.002	0.002	0.003	0.003	0.003	0.003
∑cat	4.000	0.000	15.092	15.004	15.002	15.003	7.985	0.013	13.845	0.100	18.942	0.264	5.011	0.058		0.009	12.023	0.156
F			0.069	0.021	0.025	0.040	0.031	0.022	0.021	0.043	0.058	0.055					0.077	0.069
X_{Mg}	4.971	0.702	1.609	1.772	1.660	1.771			0.456	0.529	12.601	3.205						

Supplementary material

Click here to download Table: SM2.pdf

SM2: Representative microprobe analyses for metabasite sample RMT4A

	Cpx		Opx		Gln 2 ***		Act		Ep		Ms***		Ms****	Chl		Ab		An		Ttn	
	av(9)	±σ	av(6)	±σ	av(53)	±σ	av(5)	±σ	av(20)	±σ	av(6)	±σ	av	av(24)	±σ	av(3)	±σ	av(6)	±σ	av(3)	±σ
SiO_2	52.86	1.88	54.11	4.24	57.78	0.70	53.21	3.96	37.48	0.42	39.88	5.28	46.28	29.85	1.74	68.37	0.71	44.01	1.67	30.41	0.27
TiO_2	1.05	0.16	1.17	0.20	0.19	0.10	0.24	0.32	0.05	0.03	0.05	0.05	0.03	1.42	6.83	0.03	0.02	0.19	0.18	39.64	0.53
Al_2O_3	3.06	0.69	4.15	0.15	9.80	1.05	3.59	3.41	23.92	2.01	28.22	2.83	38.68	18.52	3.39	19.99	0.35	36.13	1.21	1.22	0.10
Cr_2O_3	0.18	0.17	0.43	0.08	0.03	0.09	0.06	0.07	0.05	0.02	0.04	0.02	0.00	0.06	0.03	0.01	0.01	0.01	0.02	0.00	0.00
FeOt	6.56	0.36	6.10	0.37	10.74	0.80	9.57	1.15	12.22	1.45	5.91	2.65	0.56	15.35	3.58	0.12	0.27	0.45	0.31	0.55	0.21
MnO	0.16	0.07	0.15	0.02	0.16	0.03	0.22	0.03	0.12	0.04	0.07	0.05	0.00	0.30	0.08	0.01	0.01	0.02	0.02	0.04	0.02
MgO	15.15	0.37	14.01	1.25	10.92	0.50	17.43	1.41	0.23	0.60	0.36	0.65	0.06	21.22	4.62	0.04	0.27	0.22	0.48	0.00	0.00
CaO	20.30	1.32	19.58	2.79	1.01	0.43	11.46	0.63	22.43	0.53	21.27	4.27	1.16	1.19	5.10	0.20	0.41	18.66	1.32	27.99	0.17
Na_2O	0.40	0.04	0.49	0.08	6.36	0.32	0.56	0.14	0.01	0.01	0.55	1.63	0.20	0.03	0.04	11.91	0.51	0.76	1.00	0.01	0.02
K_2O	0.01	0.01	0.01	0.01	0.02	0.02	0.05	0.06	0.01	0.01	0.04	0.06	9.95	0.01	0.01	0.04	0.05	0.03	0.04	0.00	0.01
F					0.10	0.00	0.05	0.07	0.03	0.07	0.02	0.03		0.08	0.09					0.29	0.22
Total*	99.71	0.59	100.20	3.44	97.10	4.03	96.45	11.23	96.53	5.18	96.41	17.53	96.91	88.02	25.50	100.72	2.63	100.47	6.24	100.14	1.54
Si	1.956	0.077	2.000	0.160	8.002	0.075	7.602	0.455	2.969	0.041	3.075	0.298	6.012	5.657	0.401	2.377	1.320	2.027	0.059	3.947	0.011
Al	0.133	0.030	0.181	0.006	1.620	0.210	0.614	0.593	2.231	0.148	2.574	0.262	5.922	4.190	0.816	0.823	0.447	1.962	0.073	0.187	0.017
Ti	0.029	0.004	0.033	0.006	0.020	0.010	0.036	0.037	0.003	0.001	0.003	0.003	0.003	0.142	0.682	0.004	0.005	0.007	0.006	3.870	0.022
Cr	0.005	0.005	0.013	0.002			0.007	0.008	0.003	0.001	0.002	0.001	0.000	0.009	0.005	0.000	0.000	0.000	0.001	0.000	0.000
Fe^{3+}	0.009	0.025	0.014	0.024	0.119	0.099	0.208	0.211	0.810	0.105	0.386	0.183		1.973	0.473	0.003	0.003	0.009	0.014	0.048	0.018
Fe^{2+}	0.193	0.028	0.175	0.024	1.288	0.098	0.964	0.081	0.000	0.000	0.000	0.000	0.060	0.493	0.118					0.012	0.005
Mn	0.005	0.002	0.005	0.001	0.019	0.004	0.027	0.004	0.008	0.003	0.005	0.003	0.000	0.049	0.013	0.000	0.000	0.001	0.001	0.004	0.003
Mg	0.835	0.018	0.771	0.058	2.254	0.099	3.712	0.244	0.027	0.070	0.041	0.072	0.011	6.075	1.352	0.001	0.002	0.015	0.033	0.000	0.000
Ca	0.804	0.050	0.774	0.097	0.150	0.063	1.756	0.078	1.904	0.044	1.767	0.358	0.161	0.178	0.724	0.012	0.007	0.921	0.069	3.892	0.007
Na	0.028	0.003	0.035	0.006	1.698	0.079	0.155	0.039	0.002	0.002	0.077	0.226	0.051	0.010	0.012	0.820	0.412	0.067	0.088	0.003	0.004
K	0.000	0.000	0.000	0.000	0.004	0.002	0.008	0.010	0.001	0.001	0.004	0.006	1.649	0.003	0.002	0.002	0.001	0.002	0.002	0.001	0.001
∑cat	4.000	0.000	4.000	0.000	15.004	0.044	15.053	0.026	7.977	0.019	7.954	0.047	13.874	18.784	1.437	4.027	2.219	5.015	0.021	12.006	0.009
F					0.004		0.032	0.031	0.008	0.018	0.005	0.007	0.000	0.047	0.050					0.118	0.090
X_{Mg}	0.812	0.391	0.815	0.707	0.636	0.503	0.794	0.751					0.155	0.925	0.920						

Supplementary material

Click here to download Table: SM3.pdf

SM3: Representative microprobe analyses for metabasite sample RMT7B

	Opx		Gln cores***		Gln rims***		Czo	Chl	Ttn
	av(4)	±σ	av(10)	±σ	av(5)	±σ	av	av	av
SiO_2	54.24	0.26	58.52	0.52	57.93	1.28	45.42	28.99	30.16
TiO_2	0.05	0.05	0.15	0.04	0.16	0.04	0.01	0.02	38.90
Al_2O_3	3.35	0.28	9.28	0.39	9.59	0.55	27.70	18.80	1.20
Cr_2O_3	0.12	0.04	0.08	0.04	0.06	0.05	0.06	0.11	0.00
FeOt	10.40	0.32	11.14	0.01	11.74	0.68	3.42	16.58	0.75
MnO	0.28	0.06	0.20	0.04	0.22	0.06	0.05	0.26	0.06
MgO	10.14	0.31	10.90	0.00	10.94	0.50	2.86	23.46	0.00
CaO	15.43	0.55	0.86	0.23	1.35	0.44	14.94	0.05	27.93
Na_2O	5.33	0.38	6.48	0.26	6.20	0.27	2.29	0.00	0.00
K_2O	0.07	0.04	0.02	0.01	0.03	0.02	0.06	0.01	0.02
F			0.10	0.14	0.06	0.09	0.06	0.18	0.22
Total*	100.35	0.66	100.14	0.30	100.74	0.62	97.07	89.87	99.59
Si	1.985	0.021	8.074	0.047	7.946	0.166	3.398	5.558	3.952
Al	0.145	0.012	1.509	0.068	1.556	0.078	2.442	4.248	0.186
Ti	0.001	0.001	0.016	0.005	0.016	0.004	0.001	0.003	3.835
Cr	0.004	0.001	0.008	0.004	0.007	0.005	0.003	0.017	0.000
Fe^{3+}	0.260	0.061	0.000	0.000	0.216	0.484	0.214	2.127	0.066
Fe^{2+}	0.058	0.058	1.285	0.003	1.131	0.439	0.000	0.532	0.016
Mn	0.009	0.002	0.023	0.004	0.026	0.007	0.003	0.042	0.007
Mg	0.553	0.015	2.242	0.006	2.236	0.098	0.319	6.703	0.000
Ca	0.605	0.021	0.128	0.034	0.198	0.065	1.197	0.010	3.922
Na	0.378	0.025	1.733	0.065	1.650	0.076	0.333	0.000	0.000
K	0.003	0.002	0.003	0.002	0.004	0.003	0.005	0.001	0.003
∑cat	7.583	0.974	15.020	0.012	14.979	0.108	7.926	19.242	12.028
F			0.044	0.062	0.024	0.038	0.014	0.111	0.092
X_{Mg}			0.636	0.000	0.674	0.110			

Supplementary material

Click here to download Table: SM4.pdf

SM4: Representative microprobe analyses for metabasite sample RMT5B

	Ep		Phn		Chl		Ab	Ttn
	av(2)	±σ	av(4)	±σ	av(4)	±σ	av	av
SiO_2	37.30	0.09	50.32	0.34	29.86	0.96	67.88	31.07
TiO_2	0.04	0.06	0.04	0.01	7.19	16.03	0.00	35.87
Al_2O_3	21.74	0.17	25.75	0.54	16.47	7.60	20.25	2.90
Cr_2O_3	0.06	0.04	0.07	0.04	0.09	0.11	0.00	0.01
FeOt	14.26	0.40	4.18	1.11	9.90	5.34	0.10	0.67
MnO	0.20	0.03	0.02	0.02	0.25	0.15	0.00	0.00
MgO	0.00	0.00	3.96	0.45	19.62	10.99	0.01	0.00
CaO	22.06	0.52	0.13	0.12	5.73	12.56	0.37	28.19
Na_2O	0.02	0.02	0.09	0.02	0.01	0.02	12.08	0.04
K_2O	0.03	0.01	10.45	0.22	0.24	0.30	0.06	0.09
F	0.00	0.00	0.08	0.09	0.17	0.32		0.73
Total*	95.72	1.34	95.02	2.95	89.45	54.34	100.74	99.26
Si	2.998	0.008	6.808	0.055	5.351	0.728	2.952	4.059
Alt	2.060	0.027	4.106	0.075	3.684	1.812	1.038	0.446
Ti	0.003	0.004	0.004	0.001	0.708	1.576	0.000	3.526
Cr	0.004	0.002	0.007	0.005	0.013	0.016	0.000	0.001
Fe^{3+}	0.959	0.022			1.266	0.699	0.004	0.059
Fe^{2+}	0.000	0.000	0.473	0.125	0.317	0.175		0.015
Mn	0.014	0.002	0.002	0.003	0.041	0.025	0.000	0.000
Mg	0.000	0.000	0.798	0.092	5.614	3.145	0.000	0.000
Ca	1.900	0.035	0.018	0.017	0.809	1.754	0.017	3.947
Na	0.003	0.003	0.024	0.005	0.003	0.004	1.018	0.011
K	0.003	0.001	1.803	0.040	0.057	0.073	0.003	0.015
∑cat	7.963	0.018	14.045	0.008	17.874	3.219	5.038	12.117
F	0.000	0.000	0.033	0.037	0.072	0.130		0.303
X_{Mg}			0.628	0.424	0.947	0.947		